PSFC/RR-10-14

Boundary Layer Heat Transport Experiments in Alcator C-Mod in Support of the FY2010 US DoE Joint Research Target

B. LaBombard, J.L. Terry, J.W. Hughes, D. Brunner, J. Payne,
M.L. Reinke, I. Cziegler, S. Zweben, R. Granetz, M. Greenwald,
I.H. Hutchinson, J. Irby, Y. Lin, B. Lipschultz, Y. Ma,
E.S. Marmar, N. Mucic, W. Parkin, S. Pierson, R. Rosati,
R. Rowan, H. Savelli, J. Stillerman, N. Tsujii,
R. Vieira, G. Wallace, D.G. Whyte, S. Wolfe,
S. Wukitch, G. Wurden, J. Zaks

Plasma Science and Fusion Center
Massachusetts Institute of Technology
Cambridge MA 02139 USA

This work was supported by the U.S. Department of Energy, Grant No. DE-FC02-99ER54512.

Boundary Layer Heat Transport Experiments in Alcator C-Mod in Support of the FY2010 US DoE Joint Research Target

B. LaBombard[1], J.L. Terry[1], J.W. Hughes[1], D. Brunner[1], J. Payne[1], M.L. Reinke[1], I. Cziegler[1], S. Zweben[2], R. Granetz[1], M. Greenwald[1], I.H. Hutchinson[1], J. Irby[1], Y. Lin[1], B. Lipschultz[1], Y. Ma[1], E.S. Marmar[1], N. Mucic[1], W. Parkin[1], S. Pierson[1], R. Rosati[1], R. Rowan[3], H. Savelli[1], J. Stillerman[1], N. Tsujii[1], R. Vieira[1], G. Wallace[1], D.G. Whyte[1], S. Wolfe[1], S. Wukitch[1], G. Wurden[4], J. Zaks[1] and the Alcator C-Mod Team

[1]MIT Plasma Science and Fusion Center, Cambridge, MA 02139 USA
[2]Princeton Plasma Physics Laboratory, P.O. Box 451, Princeton, NJ 08540 USA
[3]University of Texas, Fusion Research Center, Austin, TX 78712
[4]Los Alamos National Laboratory, Los Alamos, NM 87545 USA

September 2010

Physics-based transport models that can accurately simulate heat-flux power widths in the tokamak boundary plasma are lacking at the present time. Existing empirical scaling laws for heat-flux power widths appear to be ambiguous and not well formulated. Yet this information is of fundamental importance for ITER and of utmost importance for DEMO, where the lifetime of the first-wall will be a limiting factor. Recognizing this gap in understanding, Alcator C-Mod, in coordination with DIII-D and NSTX, conducted experiments in FY2010 aimed at characterizing divertor heat flux 'footprints' and their connections to conditions in the boundary and core plasmas. This research was performed in support of a Joint Research Target (JRT) established by the US DoE Office of Fusion Energy Sciences.†

This report summarizes Alcator C-Mod's contributions to the JRT and constitutes completion of the FY2010 milestone.

---

†**US DoE Office of Fusion Energy Sciences JRT for FY2010**: Conduct experiments on major fusion facilities to improve understanding of the heat transport in the tokamak scrape- off layer (SOL) plasma, strengthening the basis for projecting divertor conditions in ITER. The divertor heat flux profiles and plasma characteristics in the tokamak SOL will be measured in multiple devices to investigate the underlying thermal transport processes. The unique characteristics of C-Mod, DIII-D, and NSTX will enable collection of data over a broad range of SOL and divertor parameters (e.g., collisionality, beta, parallel heat flux, and divertor geometry). Coordinated experiments using common analysis methods will generate data that will be compared with theory and simulation.

1. Project Overview

The physics of boundary layer heat transport and its associated 'heat flux footprint' at divertor strike-point regions is of fundamental importance for the attainment of magnetic fusion energy production, yet it is poorly understood. Recognizing this fact, Alcator C-Mod initiated an aggressive program in FY2009 aimed at contributing to this key science area, first by developing an extensive array of heat flux instrumentation for C-Mod's outer divertor strike point region and second by performing dedicated experiments to explore boundary layer heat transport. This program was designed to not only support the FY2010 DoE JRT milestone but also to expand the breadth of C-Mod's boundary layer research capabilities.

1.1 Time-line of JRT research activities

June 25, 2008 – Initial planning meeting for C-Mod's new outer divertor heat flux instrumentation, targeting installation during the FY2009 extended maintenance break

July 2008 to May 2009 – Extended C-Mod maintenance break. Divertor heat-flux instrumentation, 'ramped tiles' and IR camera systems installed; new CPCI-based data acquisition system and infrastructure installed for embedded sensors and Langmuir probes.

July 2009 – Commissioning of new divertor heat flux instrumentation (MP#557)

August to October 2009 – Initial L-mode heat flux experiments (MP#570)

October 8, 2009 – FY2010 JRT milestone officially established by US DoE OFES

November 2009 to February 2010 – Development of C-Mod's IR image stabilization algorithms and heat flux analysis software packages; Development of C-Mod EDA H-mode mini-proposal (MP#591), in coordination with NSTX and DIII-D

February 9 and 11, 2010 – DIII-D joint facility experiments (D3DMP No. 2010-62-02), including DIII-D/C-Mod 'similarity discharges'

February 12 to March 10, 2010 – C-Mod EDA H-mode joint facility experiments (MP#591), including DIII-D/C-Mod 'similarity discharges'

April to June 2010 – C-Mod up-to-air maintenance break. Refurbished and installed improved divertor 'ramped tiles' and heat flux sensor arrays. New ramped-tile Langmuir probes installed. Initial analysis of EDA H-mode data performed; data published at PSI and HTPD conferences.

July 2010 – C-Mod EDA H-mode data ported to modelers (CPES, Lodestar, LLNL) and distributed to JRT team.

July to August 2010 – Second round of L-mode heat flux experiments with repaired/improved diagnostic set (MP#570)

August 2010 – Final set of EDA H-mode experiments (MP#591)

October 2010 – Final JRT report (including this document) sent to US DoE OFES

1.2 Key results

- Divertor heat flux profiles exhibit a two zone structure: a narrow heat flux channel near the strike point (FWHM ~ 2 mm) and a tail in the far scrape-off layer, similar to other tokamaks (section 5.1).

- C-Mod's heat flux widths challenge empirical scalings that are currently used to project to ITER. Widths based on Kirnev *et al*. [1] are a factor of ~4 too small while those from Loarte *et al*. [2] appear to be more consistent (section 5.2).

- Yet, C-Mod's favorable comparison with the Loarte scaling appears fortuitous. Neither scaling captures the dependencies seen in C-Mod's heat flux widths, i.e., no dependence on P_{SOL} and B_ϕ, both for EDA H-modes (sections 5.4, 5.5) and ohmic L-modes (section 6).

- Contrary to transport models that assume a fixed cross-field heat diffusivity, divertor heat flux profiles are found insensitive to magnetic field line length. In plasmas where the magnetic connection length was changed by a factor of two (via magnetic topology changes), the shape of the heat flux profile remains invariant (section 5.3). These data indicate that the heat flux profile is set dynamically by the plasma; a critical-gradient model for heat transport may be needed to account for this observation. These results make contact with turbulence observations and earlier investigations of edge particle transport behaviors (section 7.1).

- Heat flux widths are found to be intimately connected to the behavior of the H-mode pedestal. This observation is clearly illustrated in discharges where the pedestal conditions evolve in time; changes in P_{SOL} do not affect the heat flux widths, while changes in pedestal conditions do (section 5.4). The quasi-coherent mode may be a key player in setting the heat flux widths in C-Mod's EDA H-modes; its importance in the particle transport channel is highlighted in edge turbulence observations (section 7.1).

- EDA H-mode heat flux widths are most strongly correlated with the stored plasma energy of the discharge and statistically uncorrelated with P_{SOL} and B_ϕ(section 5.5). A weak inverse correlation with plasma current is seen. Forcing a power-law fit to plasma current as a control variable yields an exponent (-0.17) that is much weaker than that reported from JRT experiments in DIII-D and NSTX.

- Heat flux widths in ohmic L-mode discharges are also found independent of B_ϕ, testing a factor of 2 variation in this parameter up to 8 tesla. However, unlike in EDA H-modes, a clear inverse scaling of heat flux widths with plasma current is observed (section 6).

2. Background and Motivation

ITER is expected to operate with steady-state, time-averaged SOL parallel heat fluxes (~ 1 GW m^{-2}) that are up to an order of magnitude higher than those observed in most present-day tokamaks (with the exception of Alcator C-Mod, which attains about ½ the ITER level) – a significant extrapolation from our collective operating experiences. At this power level, the width (λ_q) of power channel arriving at the divertor plate becomes a critical scaling parameter. Because of the hard engineering constraint of not exceeding ~10 MW m^{-2} steady-state power densities to material surfaces, the value of λ_q directly sets the acceptable fraction of the total scrape-off layer (SOL) power exhaust that may be allowed to come into contact with the divertor surface (f_{div}). Based on ITER design parameters and simple geometric constraints, one arrives at the relationship $f_{div} \sim 0.04\ \lambda_q$ [3], with λ_q expressed in millimeters, magnetically mapped to the outboard midplane location. Thus a 5 mm power e-folding length mandates that 80% of the SOL power must be dissipated (i. e., 1- f_{div}), in order to avoid damage to divertor surfaces and associated coolant structures (a typical projection that is assumed for ITER). This in turn demands that the ITER divertor must be operated in a partially detached regime – a regime that is not guaranteed to be compatible with the desired core plasma performance ($Q_{DT} \sim 10$). However, the empirical basis behind the extrapolation of λ_q values from present day experiments to a ~ 5 mm value in ITER is very uncertain. Of primary concern are the ambiguities in the present set of empirical scalings for λ_q with respect to major radius, scrape-off layer power density and engineering parameters such as magnetic field and plasma current [1-3].

Figures 1 and 2 serve to illustrate some of these ambiguities and to motivate further experimentation. Multi-machine scalings based on heat flux 'footprints' measured at the outer divertor surface of ELMy H-modes (Fig. 1) suggested very weak or no scaling with machine size. Power-law regression analyses yielded the expressions [2]:

$$\lambda_q^{H-1}(m) = (5.2 \pm 1.3)10^{-3} P(MW)_{div}^{0.44\pm0.04} B(T)_{\phi}^{-0.45\pm0.07} q_{95}^{0.57\pm0.16} \qquad (1)$$

$$\lambda_q^{H-2}(m) = (5.3 \pm 1.4)10^{-3} P(MW)_{TOT}^{0.38\pm0.04} B(T)_{\phi}^{-0.71\pm0.08} q_{95}^{0.30\pm0.15} \qquad (2)$$

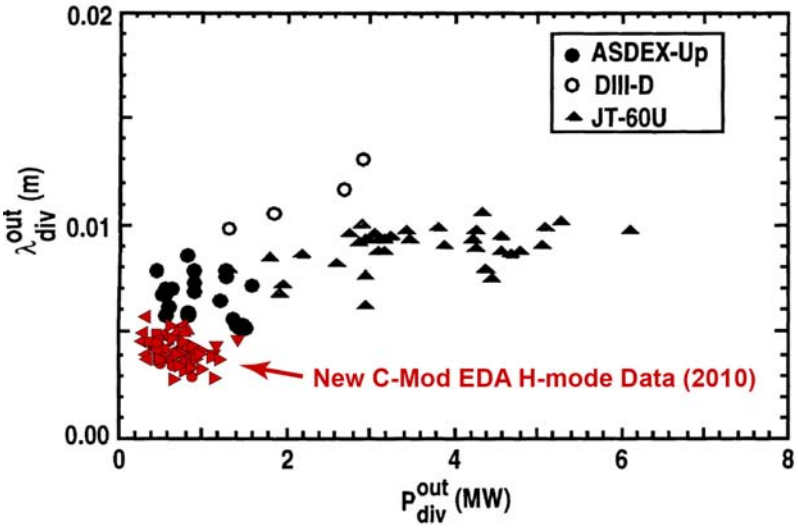

Fig. 1. Integral heat flux e-folding width measurements from ASDEX-Upgrade, DIII-D and JT-60U, as reported in [2] (black data points), suggest weak or no statistical dependence on machine size. Data from recent C-Mod experiments provide a valuable 'anchor' for machine size dependences, suggesting that there does indeed exist an imbedded machine-size scaling for the divertor heat flux footprint.

Yet, multi-machine scaling studies of the temperature e-folding lengths at the last-closed flux surface (LCFS) at the outer midplane (Fig. 2) revealed that major radius was the dominant scale parameter. These observations stand in contrast to scalings of Eqs. (1) and (2), given that the 'upstream' electron temperature profile is expected to play such a dominant role in setting the width of the power exhaust channel.

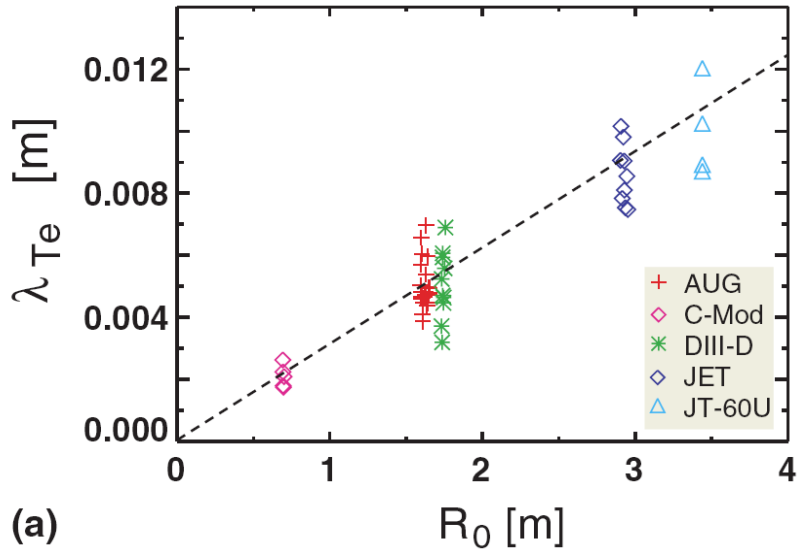

Fig. 2. H-mode electron temperature e-folding lengths near the last-closed flux surface, as measured by Thomson scattering diagnostics on five different tokamaks [4]. The dominant scaling parameter in these data was found to be major radius.

Adding to these ambiguities, detailed analyses of the power exhaust channel in JET produced yet another set of empirical scaling projections for λ_q [1]

$$\lambda_q^{cond} \propto B_\phi^{-1} P_{SOL}^{-0.5} n_{e,u}^{0.25} q_{95} R^2 \quad (3)$$

$$\lambda_q^{conv} \propto B_\phi^{-1} P_{SOL}^{-0.5} n_{e,u}^{0.25} q_{95}^{0.5} R^{1.5} \quad (4)$$

exhibiting an explicit R^2 dependence for the conduction-limited case. This scaling has been use to project to $\lambda_q \sim 4$ mm for ITER (the current design value) via an extrapolation from JET results. Nevertheless, the authors appropriately point out: "The main problem in the extrapolation … is the scaling of λ_q with the major radius, which cannot be inferred from experiments and simulations on JET alone." This ambiguous state of affairs was a strong motivator for the establishment of the FY2010 DoE JRT milestone and for Alcator C-Mod to become fully engaged in the new experiments that are described in this report. As stated plainly in the 2007 ITER Physics basis document [3]: "…there is a need for improved experimental measurements and a theory-oriented approach for making extrapolations for the target heat flux in ITER…'"

Overlayed in Fig. 1 are recent (FY2010) Alcator C-Mod measurements of λ_q from a wide range of EDA H-mode discharges [5]. These data immediately suggest that λ_q does indeed have an embedded machine-size dependence, highlighting the value of performing these experiments in C-Mod. Moreover, a new experimental infrastructure has been developed for C-Mod, which will enable boundary layer heat transport studies to be conducted beyond the FY2010 milestone.

3. Divertor Heat Flux Instrumentation

In support of the experimental program, an extensive array of divertor diagnostics was installed during C-Mod's 2009 extended maintenance period, including IR thermography, embedded calorimeters, tile thermocouples and surface thermocouples. These systems were operated from July 2009 to April 2010. In addition, a new CPCI-based data acquisition was installed, both to upgrade and expand the existing Langmuir probe data acquisition system and also to handle the new sensor signals. Custom-made analog electronics cards and backplanes where fabricated to accommodate the new range of signal types. During the most recent April-June 2010 vacuum break, a new and improved set of ramped tiles and embedded sensors were installed.

3.1 Ramped tiles, embedded sensors, IR camera – June 2009 installation

An array of embedded heat-flux sensor probes (tile thermocouples, calorimeters, surface thermocouples) combined with a new IR camera (ElectroPhysics Titanium 550M) was installed

during C-Mod's 2009 maintenance period (see Fig. 3). This camera, now sold as the FLIR SC7000, was supplied through C-Mod's collaboration with LANL, DoE Award DE-AC52-06NA25396. Instrumented tiles on the outer divertor consist of two vertical columns, tilted in the toroidal direction by ~2 degrees and 'ramped up' by 2 mm relative to standard tiles. This ensures that the instrumented tiles will not be shadowed by misalignments that are extremely difficult to avoid since field lines strike the C-Mod targets at grazing angles as small as 1º. It also increases the thermal load to the ramped tiles, improving signal-to-noise for sensor-based diagnostics.

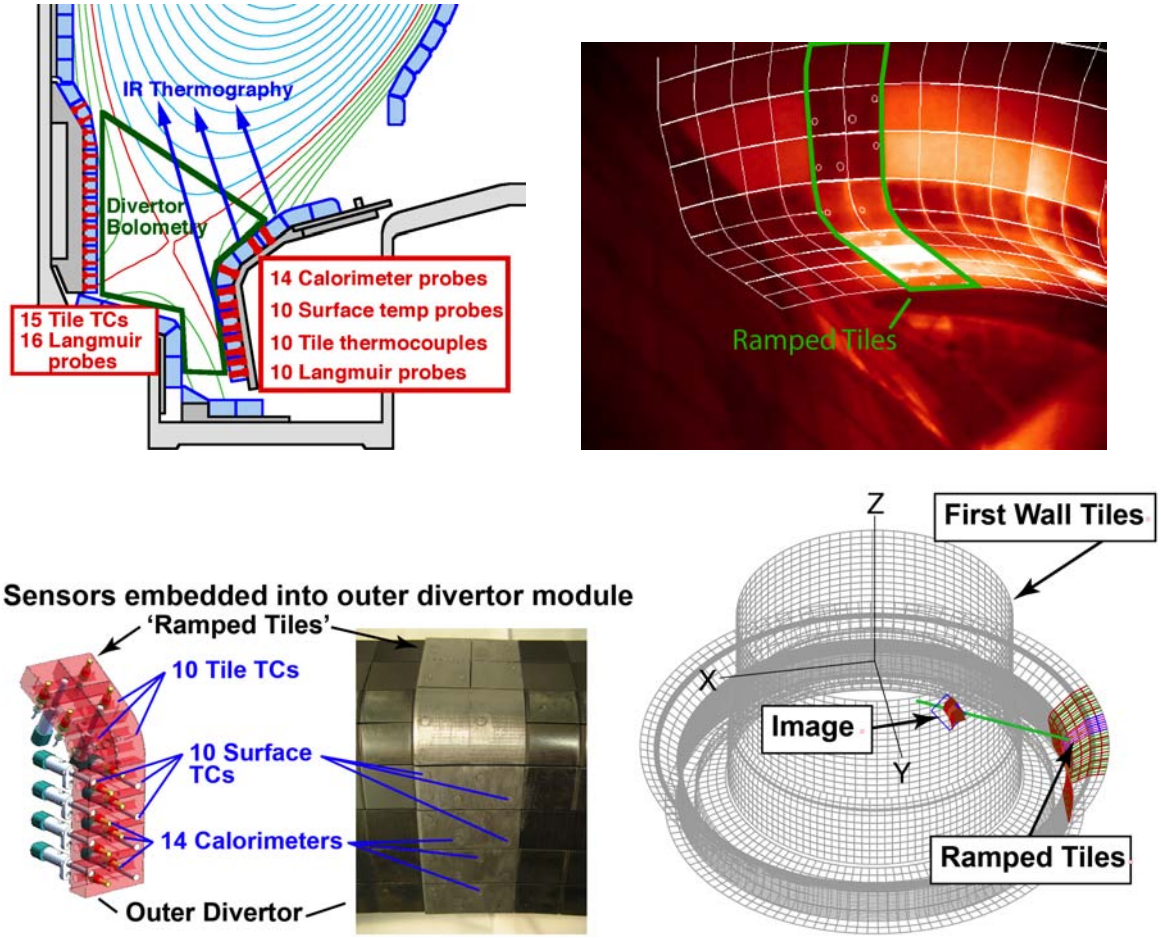

Fig. 3. Divertor heat flux diagnostic set installed during the 2009 extended maintenance period. An array of calorimeters plus surface and tile temperature sensors is embedded into two vertical columns of 'ramped tiles' on a sector of the outer divertor (poloidal cross-section in top left panel, image in bottom left panel). Langmuir probes (indicated in red) are located in a different sector, displaced 90 degrees toroidally. IR camera/periscope system views a portion of the outer divertor and ramped tiles at an oblique angle (top right panel). A virtual 3-D model of C-Mod's first-wall tiles and periscope location is used to generate an artificial image (bottom right panel), yielding a reference tile grid for image alignment (seen projected onto the IR image in the upper right panel).

The IR camera views the ramped tiles by looking both down and in the toroidal direction from a periscope [6], which is located in a vertical port ~90 degrees away. An example image and the schematic viewing geometry are shown in Fig. 3. IR thermography is challenging in C-Mod with its shiny, low emissivity tile surfaces and oblique observations angles [7] – an environment that is similar to ITER. Additional complications include low-Z surface films (e.g. boron) that change in time and image movement due to relative machine/periscope/camera motion that routinely exceeds 20 pixels in the image. To compensate for the image movement, the overall tile pattern is used as a landmark to numerically stabilize the image (see section 4.1), necessitating the wide field-of-view seen in Fig. 3. Nevertheless, the camera/periscope system resolves ~1 mm scale features on the ramped-tile surfaces. In-situ cross calibrations of the IR emission with the embedded thermocouples are performed after each shot while the tiles are still hot, correcting for changes in emissivity due to surface film evolution and for degradations in periscope transmission [7].

An array of 10 Langmuir probes is embedded in divertor tiles at a toroidal location that is 90 degrees away from the ramped tiles with similar poloidal spacing as the thermal sensors. These record profiles of plasma density and electron temperature at ~ 5 ms intervals and, in principal, can yield estimates of parallel heat fluxes via standard sheath models. In this way, Langmuir probe and calorimeter data can provide valuable cross-checks on the IR-inferred heat flux profiles and allow basic tests of plasma-sheath heat transmission [8].

3.2 Upgraded ramped tiles and embedded sensors – June 2010 installation

Experiments performed during the time period of August 2009 through October 2009 (MP#557 [9] and MP#570 [10]) focused on commissioning embedded heat flux sensor diagnostics and initiating boundary layer heat transport studies in ohmic L-mode discharges. Unfortunately, these experiments uncovered some problems with the embedded thermal sensor and Langmuir probe arrays. Consequently, plans were immediately formulated to address these problems via component redesign and to implement these improvements at the first vacuum-opening opportunity in FY2010. Additional improvements to the arrangement of the ramped-tile were also realized as operational experience has gained:

(1) Surface thermocouple sensors began to fail over time, appearing to lose electrical isolation of their cable shields with respect to vacuum vessel ground. The sensor signals also exhibited sensitivity to currents flowing into the divertor surface, generating an EMF that was comparable to

the thermal EMFs.

(2) Tile and calorimeter thermocouples exhibited poor thermal response times (~ 10 seconds). This was tracked to a high thermal resistance layer between the thermocouple junction and the tile/calorimeter surface.

(3) A cross-calibration of Langmuir probe sensors (indicated in Fig. 3) performed divertor strike point sweeps (MP#570) revealed that sensors 'below the nose' on the outer divertor were being shadowed by misalignments of the local divertor cassette. Langmuir probe data taken during this time period were therefore discarded and treated as unreliable [11].

(4) Concern arose that, due to heat-flux focusing effects [12], the heat flux 'footprint' on the ramped tiles might not represent the true heat flux profile on a set on axis-symmetric tiles, with the trailing edge of the ramped tile receiving an enhanced heat flux.

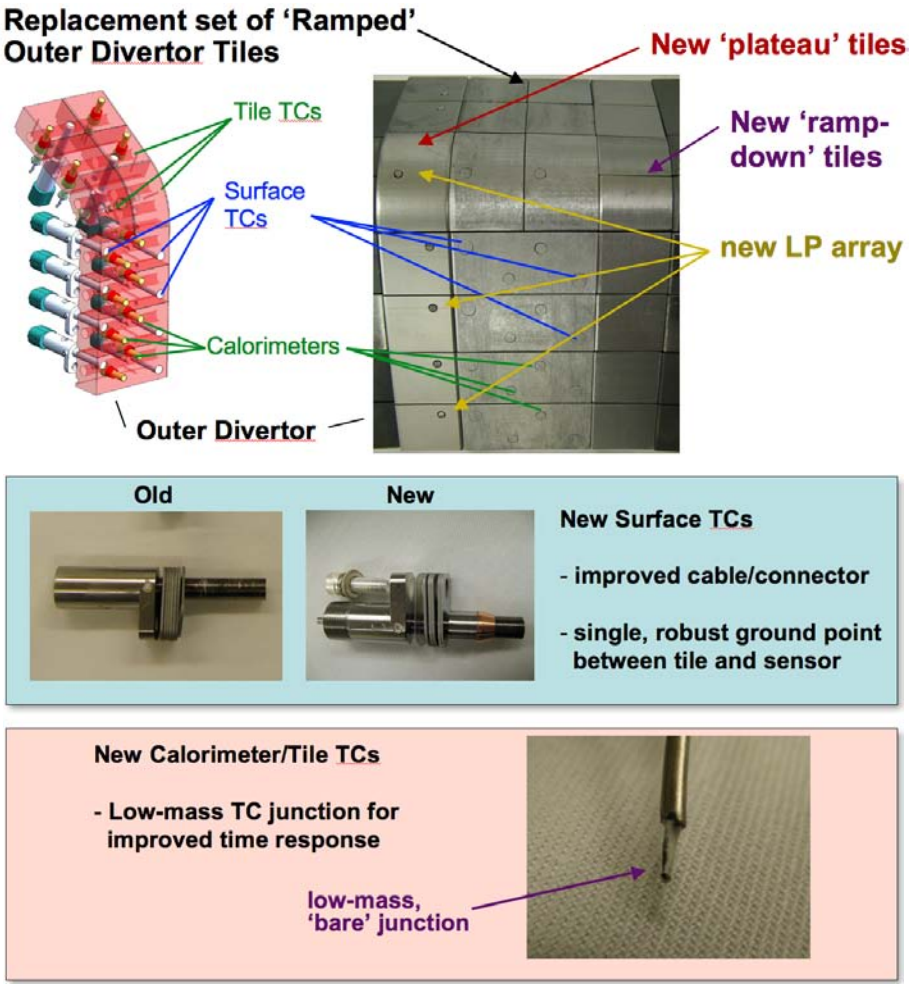

Fig. 4. A refurbished set of divertor heat flux sensors and ramped tiles were installed during April-June 2010 vacuum break, addressing a number of diagnostic issues. In addition, a new Langmuir probe array was installed on the ramped tiles.

(5) In some situations, portions of 'shadowed' regions of the outer divertor exhibited a significant amount of IR light in the camera view, indicating that this light was not originating from graybody emission but was rather some combination of reflected light and plasma emission. A reliable means for subtracting this contribution to the IR signal was desired.

To address these issues, an upgraded set of ramped-tiles and embedded sensors were installed during the April-June vacuum break (Fig. 4). The ramped tiles were extended toroidally, having a flat 'plateau' tile at the trailing edge and a 'ramp-down' tile and the leading edge of the ramp. The 'plateau' tile both eliminated concern about heat flux focusing effects on the ramp and allowed a set of Langmuir probes to be installed at this location, which would not be shadowed by divertor cassette misalignments. IR emission from the shadowed 'ramp-down' tiles provide a direct measure of the background light since these tiles are hidden with respect to parallel heat fluxes. Low-mass, bare thermocouple sensors were installed for the tile/calorimeter sensors and improvements to the grounding and cabling for the surface thermocouples were implemented (Fig. 4).

Upgrades to the IR thermography system were also instituted during this maintenance period. The most important of these was provision for a two-speed clock that externally triggered each IR image-acquisition. Since shot-to-shot cross-calibration with the embedded thermocouple systems required IR data ~30 sec after each discharge, single rate image-acquisition at the maximum full-frame rate for the camera was not practical – an enormously large data file would result. The two-speed clock upgrade allowed image-acquisition at the maximum full-frame rate (380 frames/s) for the discharge duration followed by post-discharge image-acquisition at 10 frames/s with manageable data file sizes.

4. Measurement of Heat Flux Footprints

In order to convert the raw, unstabilized IR images into time-resolved heat flux profiles across the outer divertor, a significant effort was expended during the November 2009 to January 2010 time frame to develop a suite of customized data analysis tools. The goal was to have these tools in place in time for the initial JRT experiments on EDA H-mode heat flux footprints, the first of which occurred on February 12, 2010.

4.1 IR image registration and stabilization

Due to vacuum vessel flexure during a C-Mod discharge, the IR periscope system experiences movement, causing the raw IR image to dynamically shake and shift on the order of ~20 pixels.

This effect was handled by the new data analysis software in two steps: (1) define a set of 'virtual pixels' that are fixed in space and registered with respect to the ramped tiles and (2) populate these pixels by shifting user-defined "regions-of-interest" (ROIs) in the raw images, so as to bring them into alignment, starting from the last IR image frame and proceeding back in time to the first. Image alignment at the sub-pixel level is performed by computing a 2-D cross correlation function between two edge-enhanced images, using fast Fourier transform techniques (see Fig. 5). Only translational corrections in two orthogonal dimensions were necessary; correction for image rotation was not required. Applying this image-alignment algorithm in the post-discharge processing stage provides the crucial image-stabilization. A typical time-history of image-shifts is shown in Fig. 6.

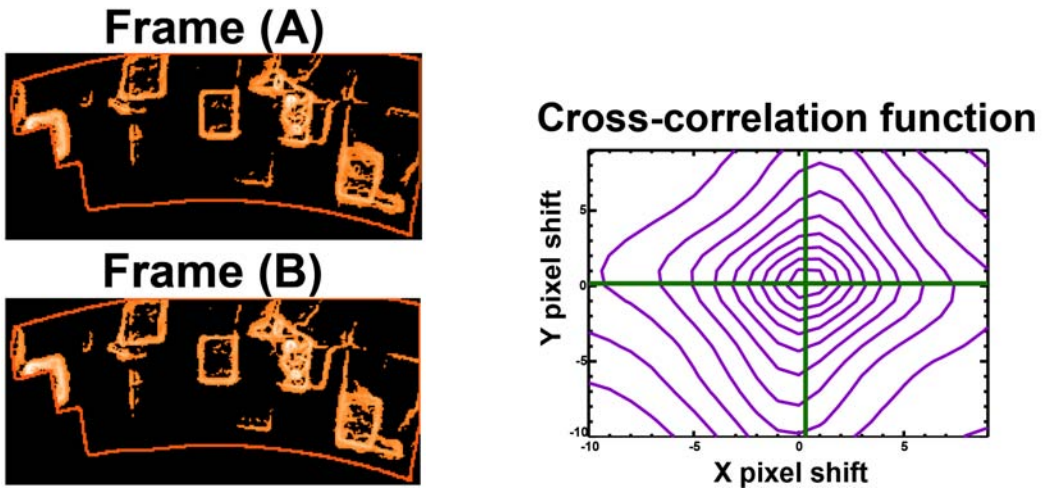

Fig. 5. A 2D cross-correlation (from FFT methods) between subsequent images is performed to correct for camera/periscope motion during a discharge. The IDL SOBEL function is used for edge enhancement, keeping only the upper 20% of pixels by intensity. Masking is performed based on predefined regions of interest (ROIs – the yellow outline shown).

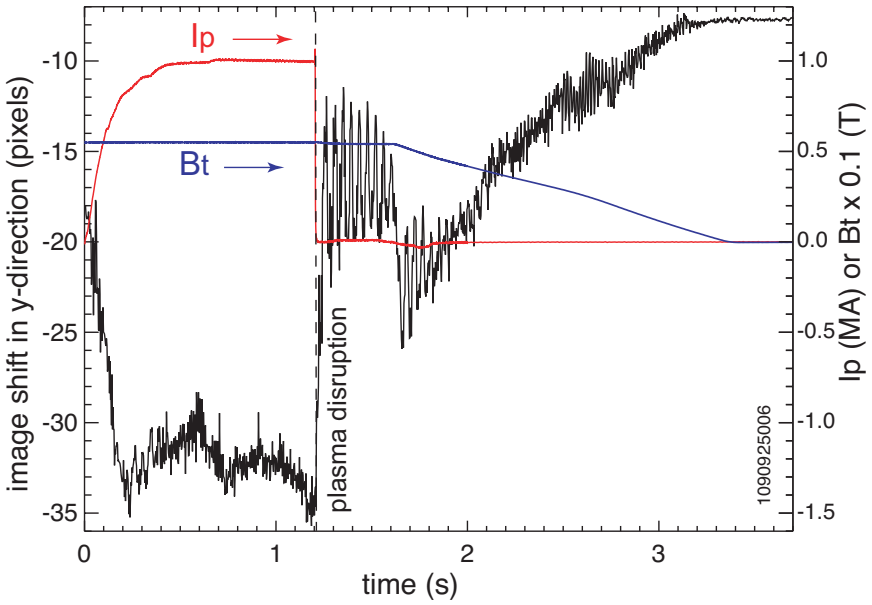

Fig. 6. Typical shifts in the "up-down" dimension needed to stabilize the IR camera image. Note the variations in the shift in response to a plasma disruption and to changes plasma current (Ip in red) and toroidal field (Bt in blue).

4.2 In situ calibration of IR thermography

The camera and viewing-periscope were initially calibrated "on the bench" using heated Mo tiles prior to deployment of the system on C-Mod. The bench calibrations showed: (1) that the clean Mo tiles emit as "graybodies" over the range of interest, i.e. follow a blackbody curve times a constant, and (2) that the camera signal, S, can be well characterized by the expression

$$S(T_{surf}.T_{camera}, \tau_{int})=Offset(\tau_{int})+\alpha(\tau_{int})B(T_{camera})+ \beta(\tau_{int})B(T_{surf}) \qquad (5)$$

where B(T) is blackbody emission within the spectral bandpass of the camera for a temperature T, α is a constant times τ_{int}, (determined by varying the temperature of the camera housing, T_{camera}, while viewing a cold plate), and β is a calibration parameter (also linear in τ_{int}) that depends on the viewed surface emissivity, the periscope transmission, the detector sensitivity, and the angle with which the surface is viewed. It can be different for each pixel. "Offset(τ_{int})" is a experimentally-determined parameter dependent only upon τ_{int}. The "graybody" emission measured in the bench calibration of a heated Mo tile is shown in Figure 7.

The IR periscope's viewing angles of the ramped-tiles (Fig. 3) are large, ranging from 35 to 80 degrees away from normal to the target surfaces. The bench calibrations also showed that the

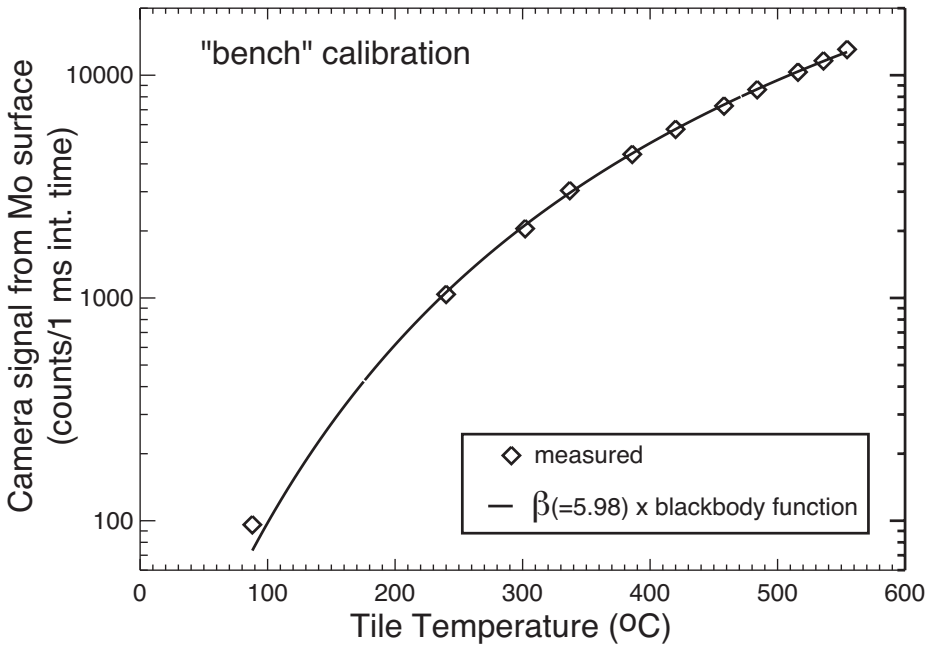

Fig. 7 Camera signal from tile surface (i.e. S-Offset-$\alpha B_{camera,periscope}$) vs temperature of a clean Mo tile measured on the "bench", compared to the graybody curve. τ_{int} in this case was 500 μs.

emissivity from a clean Mo surface increases sharply as the view angle increases beyond about 55 degrees. While this effect is present in the C-Mod measurements, another source for significant variation in surface emissivity is also present – changing low-Z surface coatings (e.g., boron). A clean Mo target surface has a low emissivity (~0.1-0.2), and the coatings increase the emissivity significantly, making in-situ calibrations necessary [7].

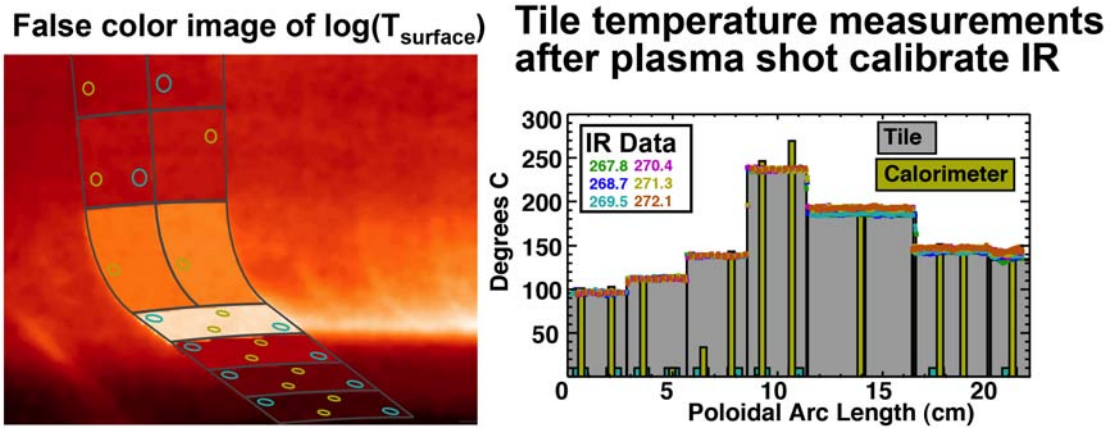

Fig. 8. Aligned and calibrated temperature image (left); IR camera calibration is based on matching the embedded sensor temperatures (right).

In-situ calibrations are produced after each tokamak pulse by taking IR camera data and tile thermocouple data for at least 25 seconds after the discharge termination, at which time the individual tiles have thermally equilibrated yet are still hot, as shown in Fig. 8.

4.3 Thermal analyses: QFLUX_1D and QFLUX_2D

1-D and 2-D finite-element heat transfer models (QFLUX_1D and QFLUX_2D) were developed to infer surface heat fluxes from surface temperature measurements and to simulate the long time thermal behavior of calorimeter and surface thermocouple sensors. These codes were benchmarked against cases where analytic solutions could be obtained and against a commercial 3-D thermal heat transport code (ALGOR [13])

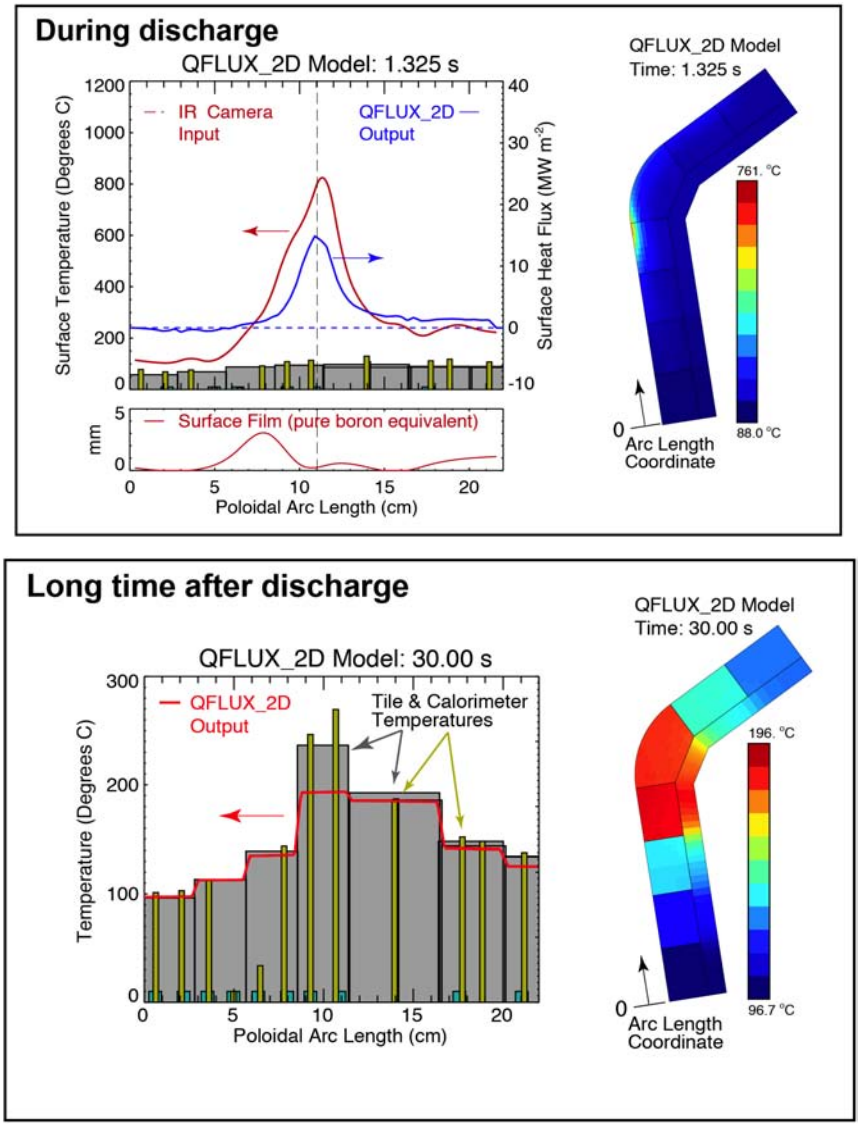

Fig. 9. Thermal analysis of ramped tiles using QFLUX_2D

QFLUX_2D contains a dimensionally accurate 2-D description of C-Mod's ramped-tile geometry, including tile gaps, at a cross-section corresponding to the ramped tile's midsection in toroidal angle. QFLUX_2D employs a fully implicit time-integration, accounts for temperature-dependent materials properties and allows a thermal resistance layer (film) profile to be specified on the tile surface. Figure 9 shows an example of a QFLUX_2D simulation. During the discharge (top panel), QFLUX_2D imposes the IR-measured surface temperatures as a time-dependent boundary condition and computes the implied surface heat flux profiles. Peak surface heat fluxes exceeding 10 MW m^{-2}, corresponding to parallel heat fluxes exceeding 200 MW m^{-2}, are routinely observed. Immediately after the discharge, the surface heat flux is set to zero and the temperatures are allowed to evolve, arriving at a tile temperature distribution that can be compared to that measured by embedded thermocouples (lower panel of Fig. 9). This technique serves as a cross-check between IR and thermocouple diagnostics. For example, some discrepancy in temperature is noted in Fig. 9, on the fourth tile from the bottom.

4.4 Surface films

Surface films can dramatically alter the relationship between surface temperature and heat flux, and if not properly considered, can lead to erroneous negative heat fluxes [14]. We have implemented a novel Fourier analysis method to estimate the thermal resistance of films: (1) compute the complex thermal impedance of a bare surface using measured temperatures and modeled heat fluxes and (2) add to this a minimal amount of surface thermal resistance to eliminate negative heat fluxes. The top panel of Fig. 9 shows the output of this computation, expressing the surface thermal resistance in terms of its equivalent thickness of a pure boron film.

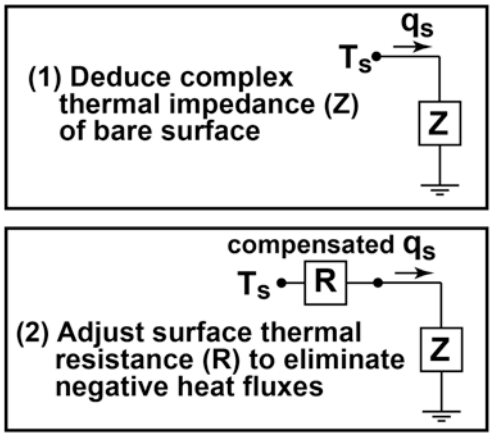

Fig. 10. Surface film compensation algorithm.

4.5 Comparison of IR and embedded sensors

Embedded calorimeters can provide an independent measurement of the discharge-integrated energy deposition profile on the ramped tile surfaces, yielding another valuable cross-check on IR thermography-inferred heat flux profiles. Prior to the installation of improved thermocouple sensors in June 2010 (see section 3.2), the calorimetry analysis had to account for the poor time-response of the thermocouples [8]. Nevertheless, good agreement between the IR thermography and calorimeter profiles has been obtained (Fig. 11), lending confidence in the IR thermography analysis that was used to study heat flux footprints in EDA H-mode discharges (reported in section 5).

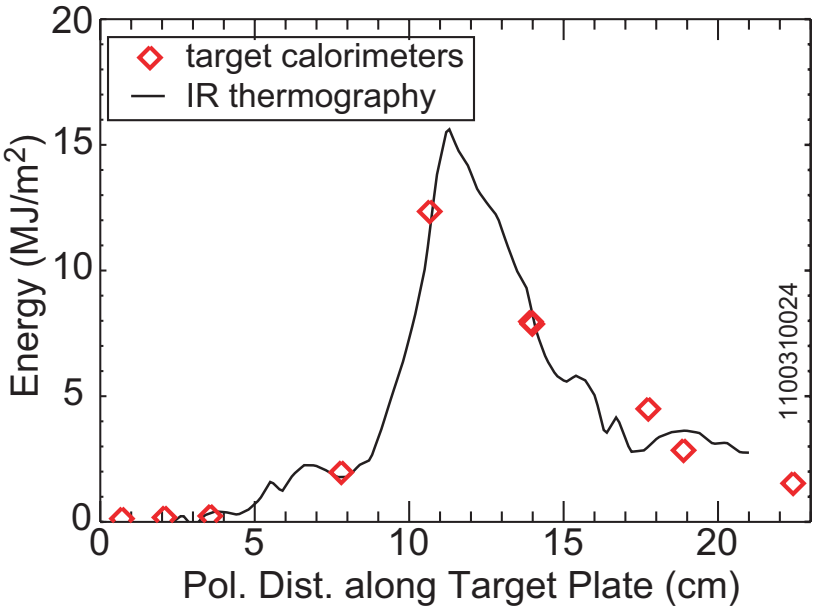

Fig. 11. Cross-check of thermal energy deposition as inferred from embedded target calorimeters and IR thermography [8].

After the June 2010 installation of the new surface thermocouples, the IR-derived temperatures could be compared directly with the lowest-noise surface thermocouple. This comparison depends on good IR image registration and stabilization since the surface TC is only 8 pixels in the image. Such a comparison is shown in Figure 12.

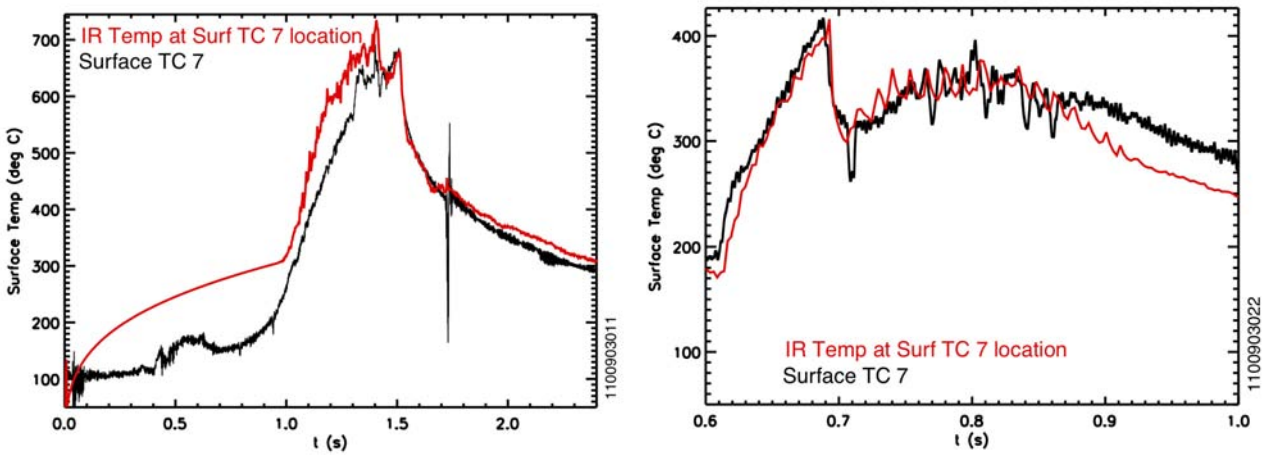

Fig. 12. Comparison of IR surface temperatures (red) and surface thermocouple temperatures (black). Left panel – The time-history over the discharge duration. (The smooth portion of the IR temperature between t~0 and t~1.0 s is interpolated, since subtraction of the "background" emission could not be performed over those times.) Right panel – Detail of a time-history comparison from a different discharge. The sharp drop in temperature at t~0.7 is the result of a L-to-H-mode transition, while the semi-periodic small changes in the IR temperature between 0.75<t<0.92 s are correlated with sawtooth crashes that are presumably expelling heat into the SOL.

4.6 Comparison of Langmuir probe and surface thermocouple inferred heat fluxes

With the new Langmuir probe array installed on the plateau section of the ramped tiles, cross-comparisons of parallel heat flux profiles from these probes and the surface thermocouples (also newly improved) could be performed. Reasonable agreement has been obtained between these diagnostics in sheath-limited and moderate recycling conditions using a standard sheath transmission factor of ~7 (Fig.10). However, some significant discrepancies have been uncovered as the plasma transitions into a high-recycling regime – a topic currently under investigation [15].

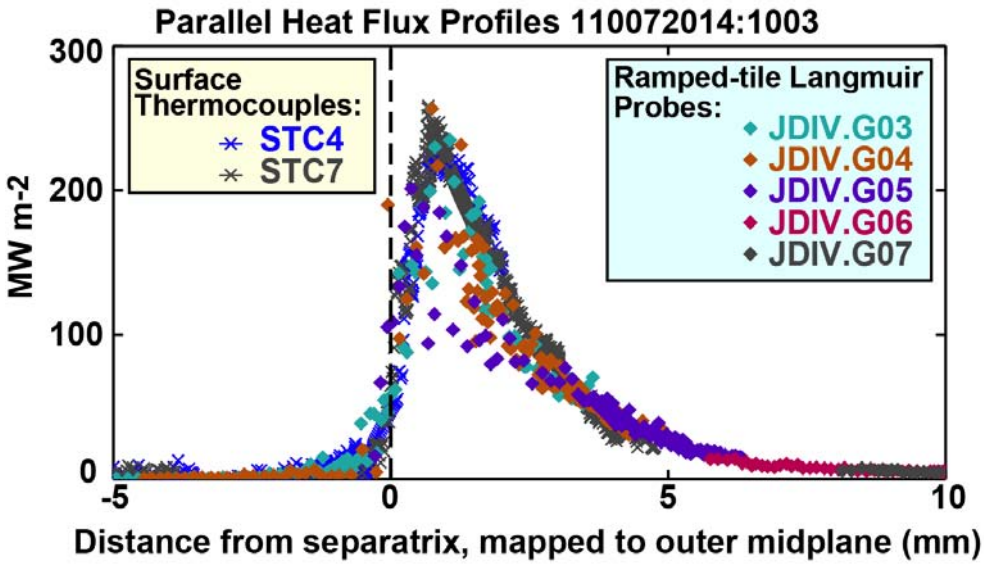

Fig. 13. Comparison of parallel heat profiles as inferred from the new Langmuir probes installed on the 'plateau tiles' (see section 3.2) and two surface thermocouples, obtained during a strike-point sweep experiment (MP#570, August 2010).

5. Heat flux footprints in EDA H-modes – MP#591

Staring in February 2010, an experimental program was begun to investigate heat flux footprints in EDA H-modes and their corresponding midplane-mapped boundary layer profiles over a wide range of parameters. C-Mod mini-proposal #591 [16] was developed for this purpose, in consultation with DIII-D and NSTX team members. It should be noted that EDA H-modes are steady-state discharges in which the pedestal is regulated by a continuous 'quasi-coherent' edge mode, rather than by a regular procession of ELMs [17]. Thus, one must be careful in relating these results to discharges whose heat flux profiles are obtained during ELMy (time-averaged) or ELM-free conditions. In addition, these discharges where operated with no extrinsic impurity seeding and with only modest divertor radiation (attached outer divertor) so as to yield a clean measure of the divertor heat flux footprints.

5.1 Experimental program – similarity discharges, I_p, B_T & P_{ICRF} scans

A total of seven run days were devoted to studying heat flux footprints in EDA H-modes, covering the engineering parameter space indicated in Fig. 14. The investigation also included 'dimensionless similarity discharges', which matched boundary layer shape and dimensionless plasma physics parameters (ν^*, ρ^*, β) with companion DIII-D discharges [18]. Five runs were performed in the February-March 2010 time frame, with the initial set of heat flux diagnostics. The

remaining two were performed in August 2010, with the refurbished diagnostic set. The DIII-D companion similarity discharges were executed on February 9 and February 11, 2010. In addition to these parameter scans, the effect of magnetic connection length on power e-folding widths was explored by comparing lower single null versus near double null discharges under otherwise identical conditions. This technique was used to help differentiate among the roles of plasma current, safety factor and connection length in empirical scalings. In all of these experiments, turbulence imaging diagnostics were employed to record fluctuation spectra in the boundary layer region (see results reported in section 7).

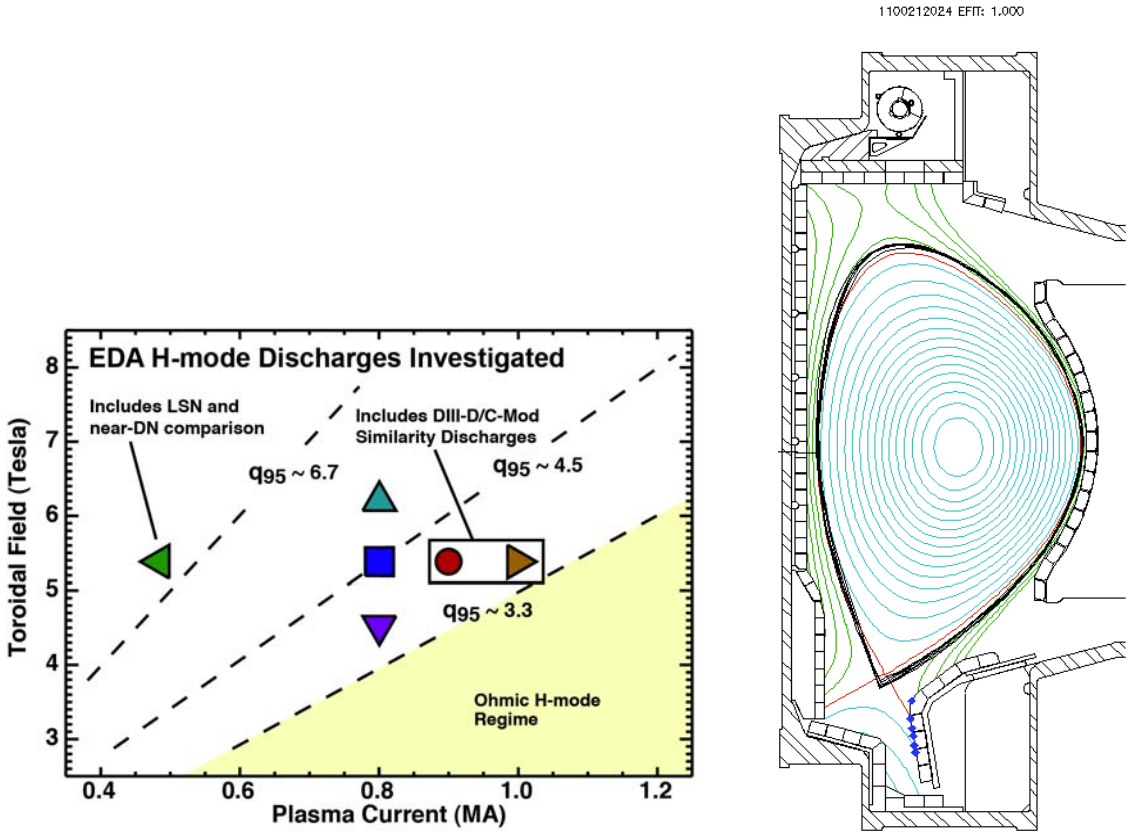

Fig. 14. Engineering parameter space explored during EDA H-mode studies (left) with boundary shape matched to DIII-D (right, with DIII-D overlay in black) – February-March 2010 (MP#591).

A good match of plasma boundary shape was been obtained between C-Mod and DIII-D for the similarity discharge set (see Fig. 14). Stable EDA H-modes were obtained at I_p = 0.9 MA and 1.0 MA. Auxiliary ICRF heating power was varied between 1 and 4 MW, with fixed and swept strike point and a variety of pedestal profiles were obtained. A comparison of C-Mod's edge temperature and density profiles with the appropriately scaled profiles from DIII-D for the similar discharges are shown in Fig. 15. Edge profiles of the dimensionless quantities ν^*, ρ^*, and β for two of the DIII-D

shots and one C-Mod shot are also shown.

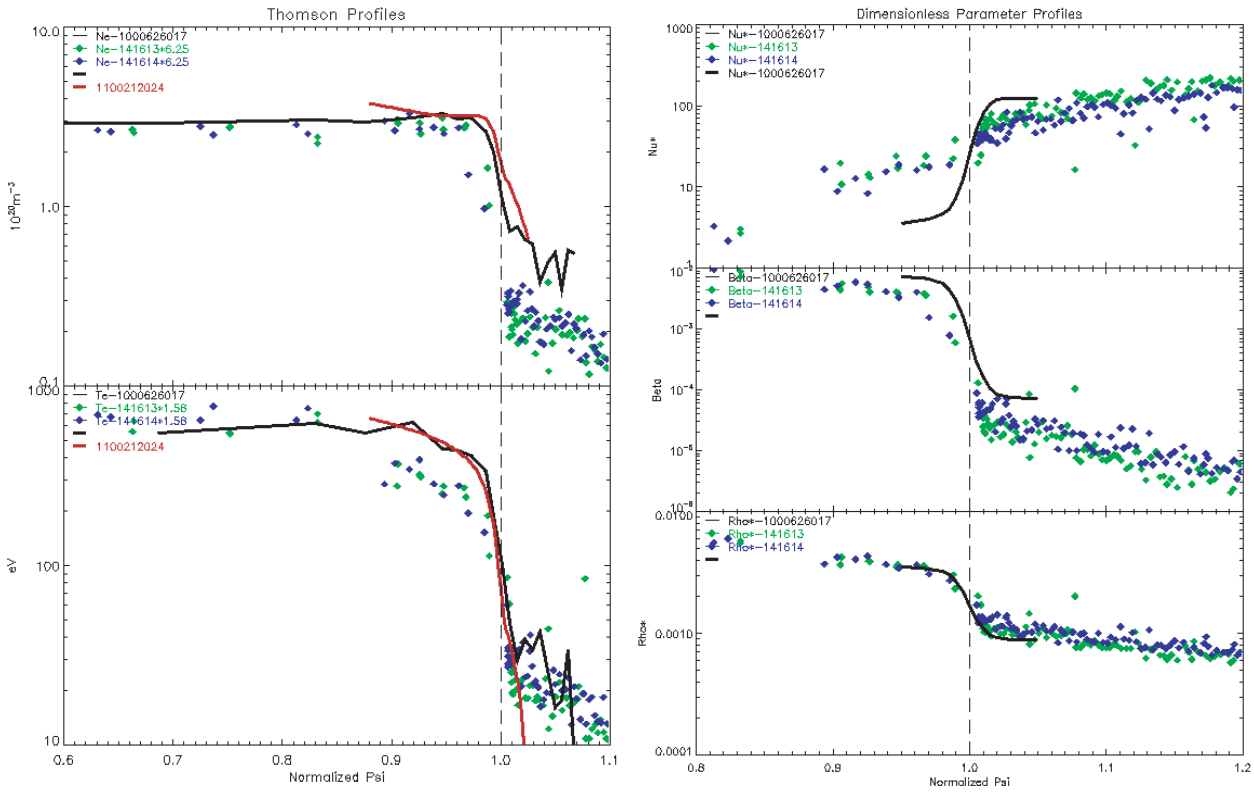

Figure 15. Left – Edge electron density and temperature profiles from C-Mod's similarity discharges (black and red lines) compared to the appropriately scaled profiles from the DIII-D similarity discharges (blue and green points). The red line is a C-Mod profile from the recent set of similarity experiments while the black line is from a C-Mod discharge (from CY 2000 [19]) that served as the target. Right — Edge profiles of the dimensionless quantities ν*, β, and ρ* *from the DIII-D (blue and green points) and C-Mod (black line) similarity discharges. The abscissa are normalized ψ.*

5.2 Heat flux profiles

Figure 16 shows results from a representative 0.9 MA, 5.4 tesla EDA H-mode discharge, with 4 MW of ICRF power (80 MHz, second-harmonic, hydrogen-minority). Radiated power from the confined plasma (P_{RAD}) is deduced from a resistive bolometer system [20], providing an estimate of the power into the scrape-off layer (P_{SOL}). Power onto the outer divertor (P_{ODIV}) is computed from the IR-inferred divertor heat flux profiles. Data from this particular discharge has been shared with external collaborators for modeling studies (section 8).

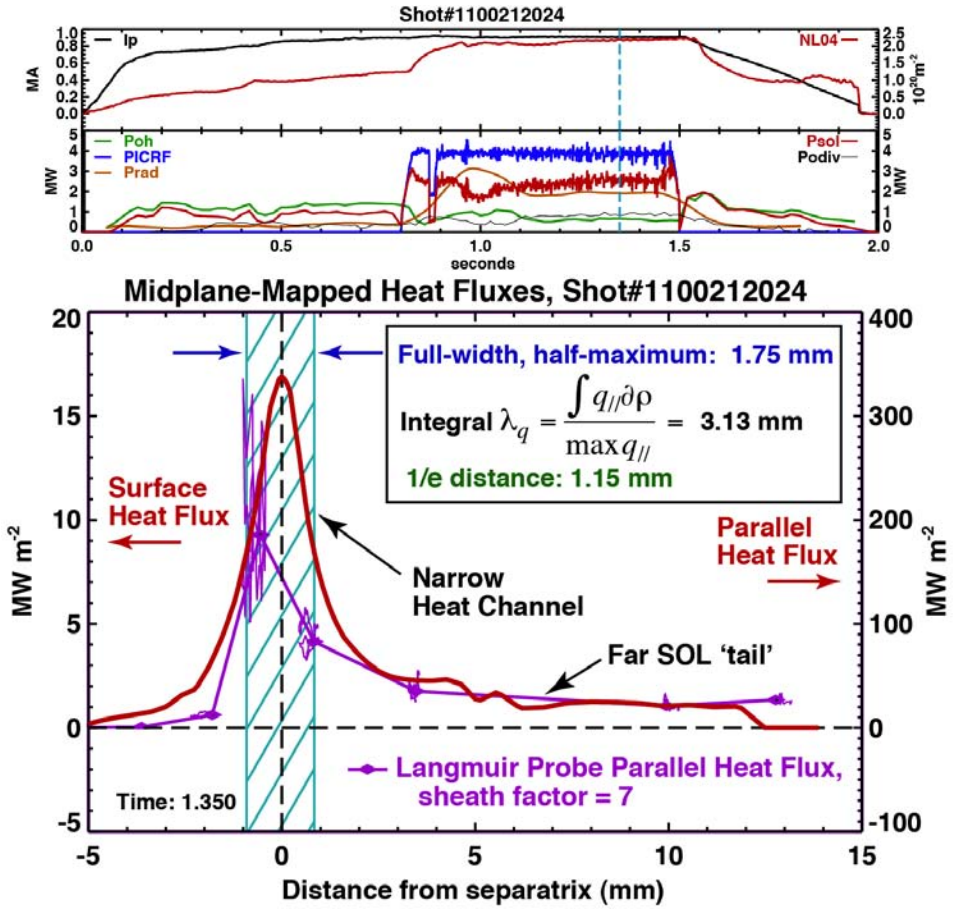

Fig. 16. Representative time traces (top panels) and a corresponding divertor heat flux footprint from a steady EDA H-mode discharge. Heat flux profiles from IR camera (red line, bottom panel) and Langmuir probe array (purple line) are shown, mapped to the outer midplane. (Note: Langmuir probe measurements near the strike point may be partially shadowed by divertor misalignments in this discharge – see section 3.2.)

Heat flux footprints are found to exhibit a two zone structure: a narrow 'power channel' near the separatrix of approximately ~ 2 mm wide (characterized by its full-width at half-maximum, FWHM), and a 'tail' that extends into the far SOL region. This behavior is similar to what has been seen in other tokamaks [21, 22]. It should be noted that the exact location of the separatrix relative to the narrow heat flux channel is uncertain, with shot-to-shot variation on the order of ~1 mm and systematic offsets on the same order. Langmuir probe data verify that the 'tail' feature in the heat-flux profile is real and not some artifact of the IR-inferred heat flux profile. Langmuir probes are not able to spatially resolve the narrow feature without sweeping the strike point, however; parallel heat fluxes in this region (> ~300 MW m^{-2}) often exceed the range in which tungsten probes can operate without melt damage.

Following the definition by Loarte [2], the integral heat flux width (also defined in Fig. 16) is found to be ~3 mm for this discharge. This value differs substantially from the scalings of Kirnev *et al*. [Eqs. (3) and (4)], which project to 0.55 mm (conduction-limited case, the one relevant here) and 1.0 mm (convection-limited case) for the discharge shown in Fig. 16. On the other hand, empirical scaling laws of Loarte *et al*. [Eqs. (1) and (2)] yield integral λ_q estimates that appear to correspond to the C-Mod observations, projecting to 5.2 mm [based on P_{DIV}] and 3.4 mm [based on P_{SOL}]. It is important to point out that if the Loarte scaling were to hold true for ITER, integral λ_q values would be ~20 mm rather than the assumed ~4 mm. However, one must be careful here. The connection of the Loarte scalings to the C-Mod data may be just fortuitous; these scalings have explicit dependencies on P_{SOL} (or P_{DIV}) and B_ϕ, and, as noted in the following sections, such scaling relationships are not observed in C-Mod's heat flux footprints.

5.3 Effect of magnetic connection length

In addition to the experiments described above, a small set of discharges (I_p = 0.5, 1.0 MA, B_T = 5.4 tesla) were run with the x-point balance changed dynamically; the magnetic equilibrium was programmed to start in lower single-null and to sweep to a double-null configuration. The goal of these experiments was to document changes in the divertor heat flux footprint as the magnetic connection length changed (a factor of ~2 longer for single-null versus double-null). One might expect that, as the connection is shortened by a factor of two, which occurs in the SOL region beyond the secondary separatrix, the heat flux profile in the common flux region would show a corresponding break in slope, yielding a shorter e-folding length there. However, as documented in Figure 17, no such response was seen in the experiment – the shapes of the heat flux profiles are robustly insensitive to the location of the secondary x-point.

This result may seem puzzling at first but is consistent with previous C-Mod observations of scrape-off layer (SOL) profiles in response to magnetic topology changes [23]: in changing from single to double-null, the electron pressure profiles in the low-field side SOL remained similar. Taken together, these observations tell us that heat transport in the SOL cannot be simply described as a fixed cross-field diffusivity that is balanced by parallel losses, which change according to magnetic connection length. Rather, the heat flux profile on the outer divertor appears to be rigidly set by 'critical gradient' phenomena on the low-field side; whether the field line connects a long

way around to the inner divertor (single-null) or a short way to the upper divertor (double null) is apparently not of primary importance.

Recognizing the significance of this observation, a follow-up set of experiments was performed on August 24, 2010, using the improved ramped tile diagnostics. Secondary x-point sweeps were performed across the lower divertor in 1.1 MA ohmic L-mode discharges and 0.5 MA EDA H-mode discharges. Care was taken to make sure that the magnetic equilibrium was swept beyond double-null into upper-single null to accommodate possible errors in EFIT mapping. Preliminary analysis indicates very similar results: the shape of the heat flux profile is found to be insensitive to the location of the secondary x-point flux surface.

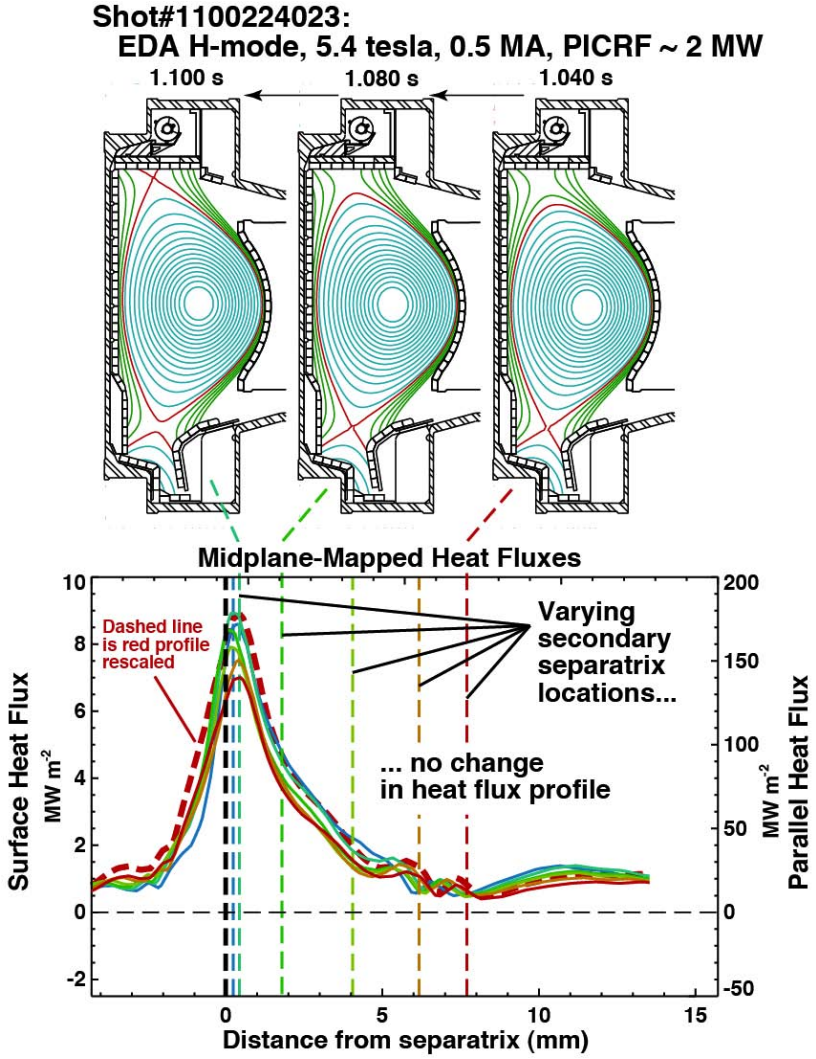

Fig. 17. Divertor heat flux profiles (bottom) obtained dynamically during a secondary separatrix sweep (top). The shape of the heat flux profiles is found to be remarkably insensitive to the change in magnetic topology. Note: Modulation in the peak heat flux is caused by changes in P_{SOL}, which varied during the sweep.

5.4 Insensitivity of λ_q to P_{SOL}, correlation with pedestal behavior

Figure 18 shows time traces from a 1.0 MA, 5.4 tesla EDA H-mode discharge that highlight some important heat flux footprint observations; these are been born out in the full data set (section 5.5). This plasma exhibited two separate EDA phases (see time-slice sample times marked EDA 1 or EDA 2), with a clear quasi-coherent mode present in both. The heat footprints and pedestal profiles corresponding to the time slices are shown in Fig. 19. During EDA 1, the ramp-up in ICRF power combined with increasing P_{RAD} resulted in a 50% modulation in the peak heat flux arriving at the outer divertor. The heat flux profiles in Fig. 19 show this modulation (red curves), yet, the shape of the normalized heat flux profiles is found to be invariant during this phase. [Note: Data from EDA1 and EDA 2 time slices have been ported to external modelers for detailed study (section 8).]

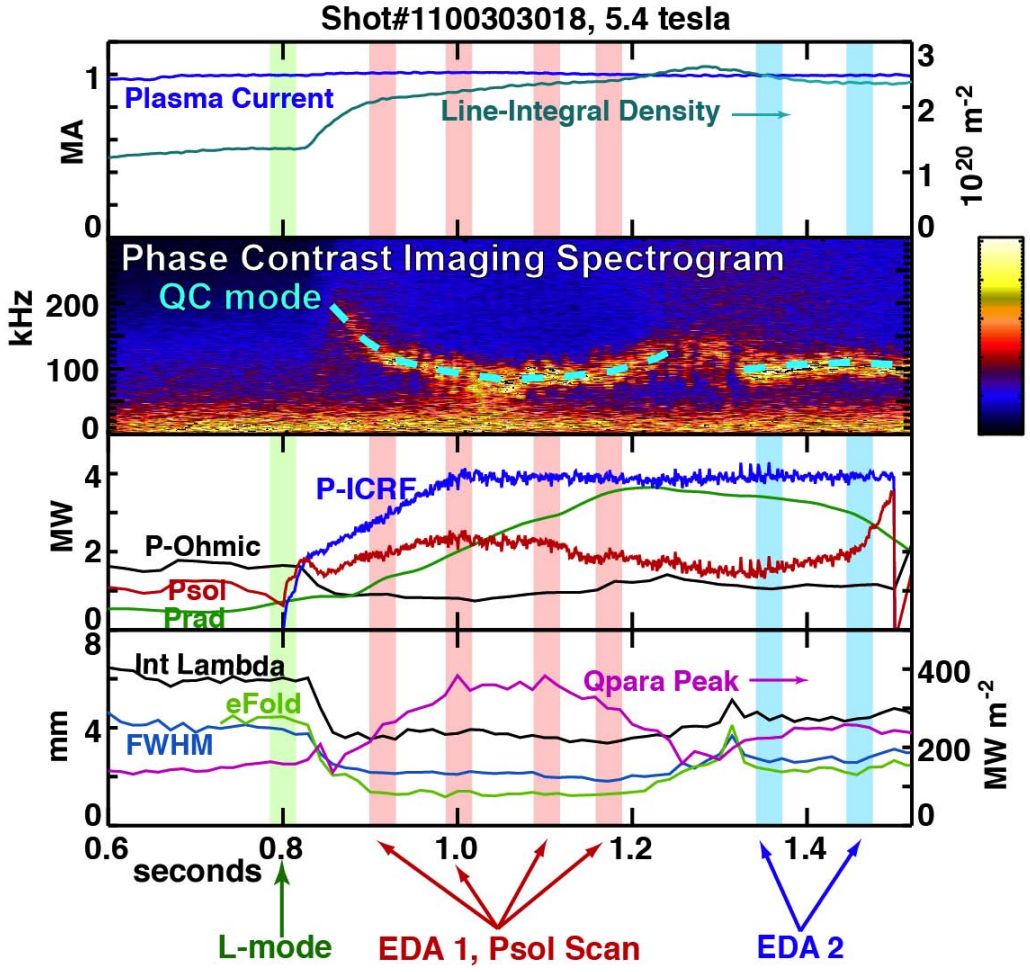

Fig. 18. Time traces from H-mode discharge with two different time-evolving EDA phases. Heat flux profiles corresponding to the time slices indicated are shown in Fig. 19.

Thus, the level of power into the scrape-off layer (P_{SOL}) does not explicitly influence the width of the heat flux footprint. Moreover, the time traces of heat flux widths in Fig. 18 change from EDA 1 to EDA 2 with essentially no change in external control parameters – integral λ_q steps up from 4 mm (EDA 1) to 5 mm (EDA 2); normalized profiles in Fig. 19 show a clear change in widths. These observations clearly confound efforts to characterize λ_q as a simple power-law function of global engineering quantities.

As shown in Fig. 19, electron pressures at the top of the pedestal were significantly reduced in the transition from EDA 1 to EDA 2. Associated with this is a flattened pressure profile in the SOL. This behavior has been noted before in C-Mod – as confinement improves, SOL pressure gradient scale lengths become shorter [24]. ASDEX-Upgrade examined similar relationships, producing an explicit power-law scaling of heat flux widths in terms of H-mode confinement factor [2]. The message here is clear: one must look to the physics of the edge transport barrier and pedestal as controlling the width of the power channel in the SOL.

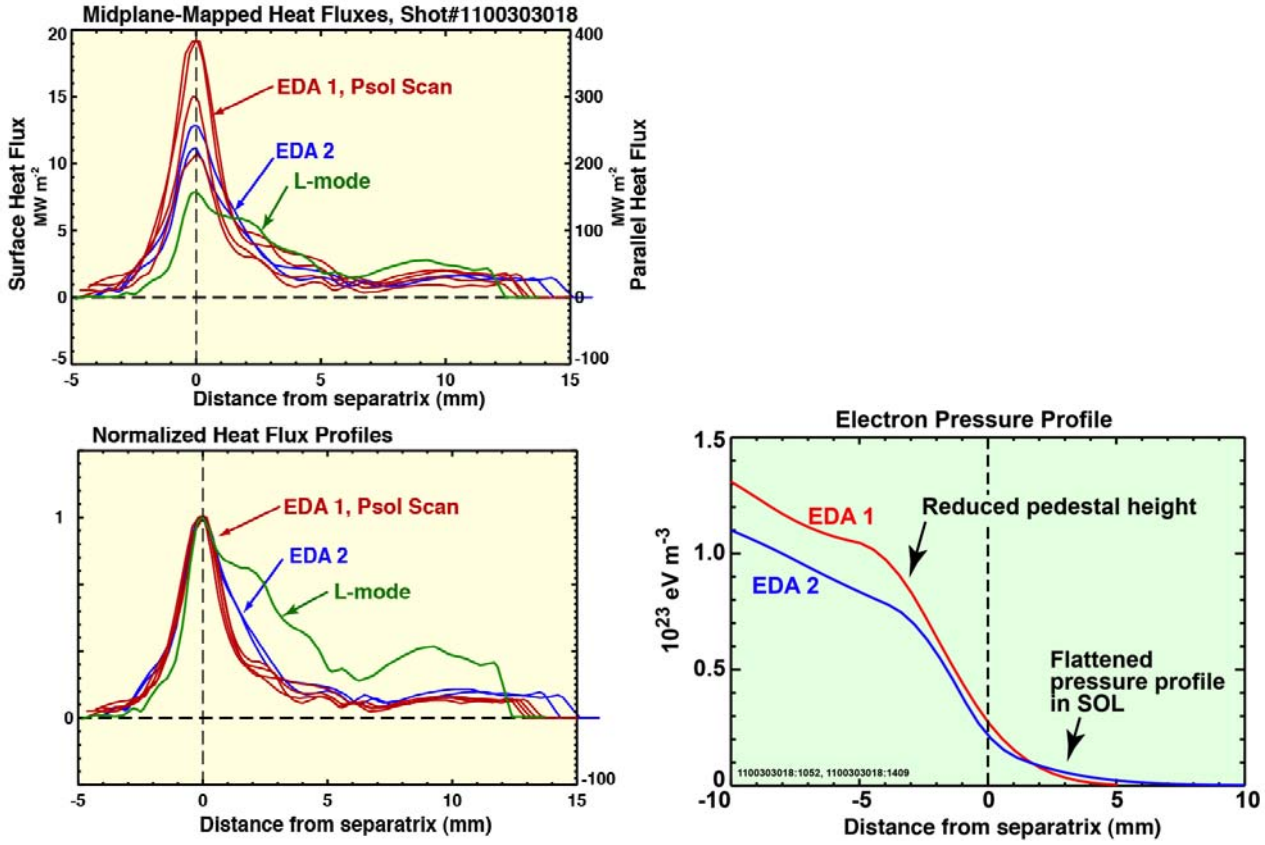

Fig. 19. Divertor heat flux profiles from L-mode, EDA 1 and EDA 2 phases (top left) and their corresponding normalized shapes (bottom left). Pedestal electron pressure profiles, averaged over EDA 1 and EDA 2 phases (bottom right).

5.5 Statistical trends

Data from the full set of EDA H-mode discharges are compiled in Fig. 20. Heat flux widths are found to systematically decrease with increasing plasma thermal energy, consistent with the above pedestal observations (note locations of EDA 1 and EDA 2 data points). Since plasma thermal energy increases roughly with plasma current squared, heat flux widths have a general tendency to decrease with increasing plasma current. While the variation of toroidal field in the present data set is modest (factor of 1.5), no explicit dependence on this parameter is evident – an observation that also makes contact with the pedestal, where pressure gradients are insensitive to toroidal magnetic field strength [25].

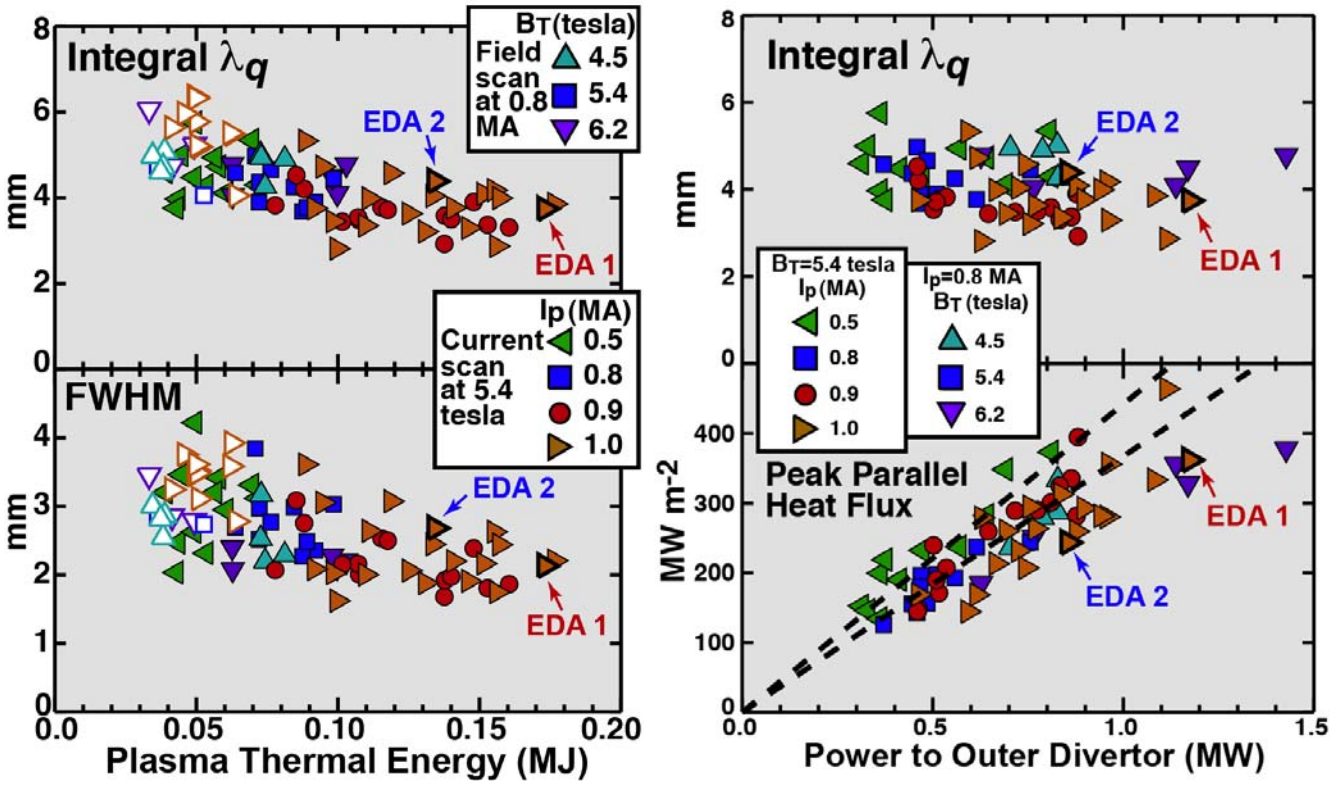

Fig. 20. Integral heat flux footprint widths are well correlated with plasma thermal energy (top left panel). Data from all conditions studied thus far follow a similar scaling, even accommodating L-mode discharges (open symbols). Full-width, half-maximum values show a similar trend with more scatter (bottom left panel). Because of these trends, heat flux widths in H-mode discharges tend to decrease with increasing plasma current. Integral widths are insensitive to power arriving at the outer divertor (top right), yielding a ~linear relationship between the peak parallel heat flux and power on the outer divertor (bottom right, with dashed lines to guide the eye). No explicit dependence on toroidal magnetic field strength is evident.

These trends can be examined more formally by statistical analysis. Here we adopt the traditional strategy of trying to describe integral λ_q in terms of a power-law function of the usual

set of regressors,

$$\lambda_q^{EDA}(mm) = C\, I_p^{\alpha}\, B_\phi^{\beta}\, P_{sol}^{\gamma}\, W_{mhd}^{\delta}\, q_{95}^{\varepsilon}\,, \qquad (6)$$

with the addition of plasma stored energy, W_{mhd}. The units of dimensional quantities in Eq. (6) are: λ_q^{EDA}[mm], I_p[MA], B_ϕ[tesla], P_{sol}[MW], and W_{mhd}[MJ]. Within this framework, regressors that are statistically the most relevant in determining λ_q can be identified by examining the χ^2 of the fit as these terms are included in the power law formula (i.e., F statistic [26]). For this data sample size, an F-test result of ~4 indicates that there is a 5% chance that the same statistical result would have

Table 1 – Results from power-law regression analysis of λ_q^{EDA} (integral λ_q in C-Mod EDA H-modes)

85 data points included			Power-law exponent					F-test result				
Case #	R^2_{mul}	C	I_p	B_ϕ	P_{sol}	W_{mhd}	q_{95}	I_p	B_ϕ	P_{sol}	W_{mhd}	q_{95}
1	0.04	4.14	-0.17					3.4				
2	0.00	4.31		0.00					0.0			
3	0.04	4.10	-0.17	0.01				3.4	0.0			
4	0.01	4.22			0.04					0.5		
5	0.05	4.06	-0.17		0.05			3.5		0.5		
6	0.01	3.78		0.06	0.05				0.0	0.5		
7	0.05	3.56	-0.17	0.08	0.05			3.5	0.1	0.6		
8	0.47	2.16				-0.27					74.5	
9	0.50	2.01	0.17			-0.31		4.6			75.9	
10	0.48	2.66		-0.13		-0.27			0.3		74.2	
11	0.50	2.61	0.17	-0.16		-0.31		4.8	0.5		75.9	
12	0.48	2.12			0.05	-0.27				0.9	74.6	
13	0.51	1.97	0.17		0.04	-0.31		4.5		0.9	75.6	
14	0.48	2.36		-0.07	0.04	-0.27			0.1	0.7	73.7	
15	0.51	2.36	0.17	-0.11	0.04	-0.31		4.6	0.2	0.6	74.9	
16	0.02	3.56					0.13					1.8
17	0.06	6.69	-0.53				-0.37	3.2				1.6
18	0.02	4.35		-0.13			0.14		0.2			2.0
19	0.21	1.28	-3.37	3.20			-3.35	18.6	15.1			16.9
20	0.03	3.42			0.06		0.14			0.7		2.1
21	0.06	6.30	-0.50		0.02		-0.34	2.5		0.1		1.1
22	0.03	3.74		-0.06	0.05		0.14		0.0	0.6		2.1
23	0.21	1.27	-3.36	3.19	0.01		-3.33	17.6	14.8	0.0		16.0
24	0.51	2.53				-0.31	-0.18				81.1	5.8
25	0.51	2.75	-0.06			-0.31	-0.24	0.1			74.3	1.2
26	0.51	2.46		0.02		-0.31	-0.18		0.0		79.8	5.4
27	0.52	1.92	-0.81	0.80		-0.29	-0.99	1.3	1.2		51.3	1.9
28	0.51	2.48			0.03	-0.31	-0.17			0.4	79.5	5.2
29	0.51	2.53	-0.02		0.03	-0.31	-0.19	0.0		0.4	73.8	0.7
30	0.51	2.25		0.06	0.03	-0.31	-0.18		0.1	0.5	78.6	5.1
31	0.52	1.82	-0.74	0.77	0.03	-0.29	-0.92	1.0	1.1	0.3	51.0	1.6

been obtained from a random regressor. Therefore, regressors with an F-test much less than 4 should be treated as statistically irrelevant.

Table 1 shows the results, considering all possible combinations of regressors in Eq. (5). The F-test results clearly identify W_{mhd} as the most relevant regressor (case #8); B_ϕ and P_{sol} are statistically irrelevant. A weak correlation with I_p is indicated (case #1). Case #24 is statistically the best, with W_{mhd} and q_{95} as the regressors. However, in all cases, the multiple regression coefficient, R^2_{mul}, is ~0.5 or less, suggesting that the power-law model expression is a poor representation of the physics and/or there are other hidden control parameters that are not being tracked. Note that cases #19 and #23 are spurious, reflecting the covariance among B_ϕ, I_p and q_{95}.

Figure 21 shows data points and corresponding regression fits for cases #1 and #8. It should be noted that the scaling of integral λ_q with respect to I_p (exponent ~ -0.17) is considerably weaker than in DIII-D [27] (exponent ~ -1.0) and NSTX [28] (exponent ~ -1.6).

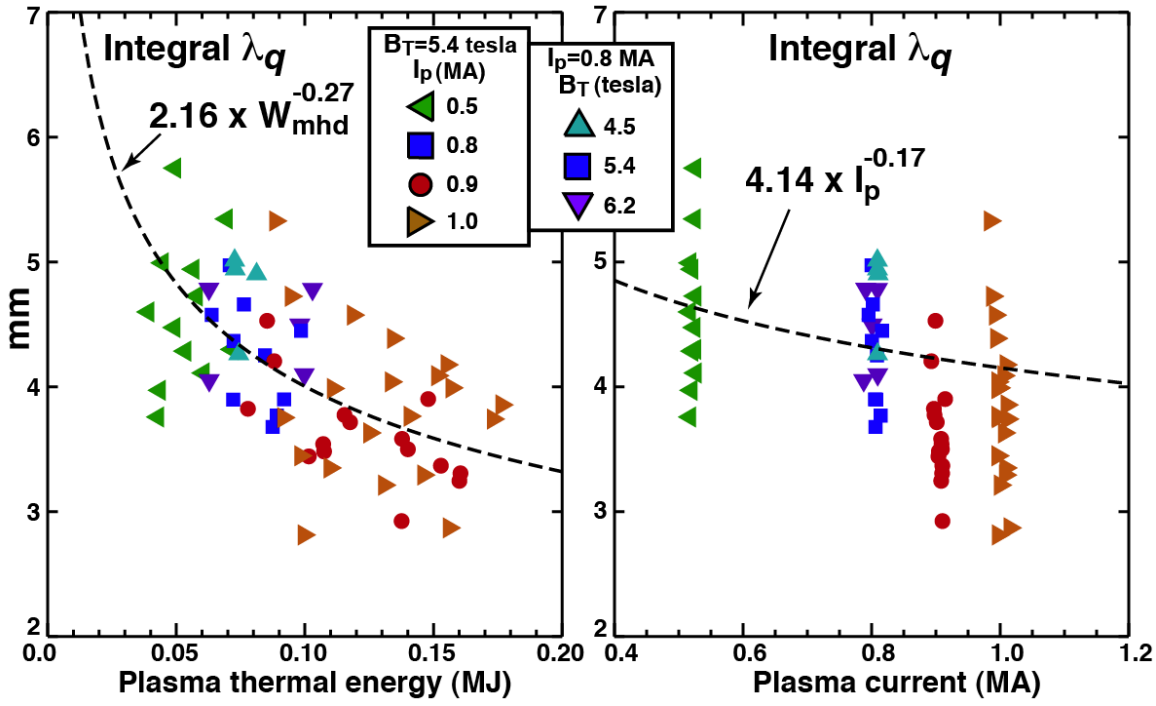

Fig. 21. Integral heat flux widths in C-Mod's EDA H-modes are better correlated statistically with plasma thermal energy (left) than plasma current (right). The power-law exponent with I_p is weak (~ -0.17), compared to that seen for ELMy H-modes in NSTX [28] and DIII-D [27].

6. Heat flux footprints in L-modes – MP#570

Because of the initial problems encountered with the embedded heat flux sensor diagnostics (see section 3.2), experimental work on MP#570 had to be postponed until after the April-June 2010 opening, when appropriate repairs and improvements could be made. Following initial re-commissioning experiments, which demonstrated that the refurbishments were quite successful, experimental work on MP#570 resumed (July 16, 2010). Four run days were devoted to MP#570 during the remaining summer run campaign, with discharges spanning a wide range of currents and fields, as shown in Fig. 22.

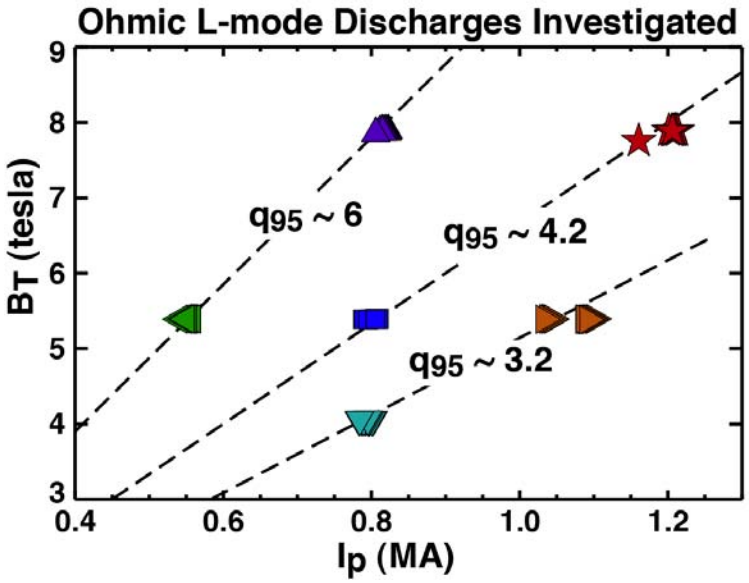

Fig. 22. Engineering parameter space explored during resumed Ohmic L-mode studies, executed on four run days – July, August 2010 (MP#570). For each current-field pair, density scans were performed, spanning normalized densities over the range 0.12 < n/n_G < 0.31.

Outer divertor strike-point sweeps were performed while holding discharge parameters otherwise unchanged. In this way, parallel divertor heat flux profiles could be recorded on embedded Langmuir probes and surface thermocouple sensors (see Fig. 4). Good agreement was obtained between these two diagnostics in low and moderate recycling regimes. However, some substantial deviations are seen in high recycling regimes, with Langmuir probes recording anomalously high heat fluxes. Such cross-comparisons among diagnostics have been found essential to weed-out potentially erroneous heat flux measurements in the data set. Although a careful analysis of the data remains to be performed, preliminary analysis reveals that, unlike in EDA H-modes, heat flux widths in ohmic L-modes exhibit a ~$1/I_p$ scaling. Figure 23 shows heat

flux profiles recorded by embedded Langmuir probes for normalized discharge densities in the range of 0.12 < n/nG < 0.17, a regime where the two diagnostics are in agreement. The corresponding e-folding distances in the common flux zone (Fig. 24), display an approximate inverse scaling with I_p and no sensitivity to magnetic field strength.

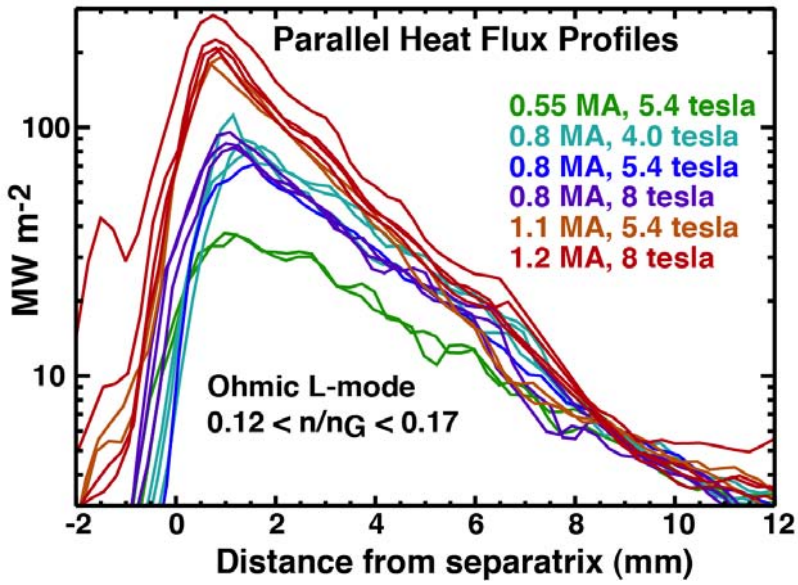

Fig. 23. Parallel heat flux profiles on the outer divertor surface as recorded by embedded Langmuir probes. Data are flux-surface mapped to the outer midplane.

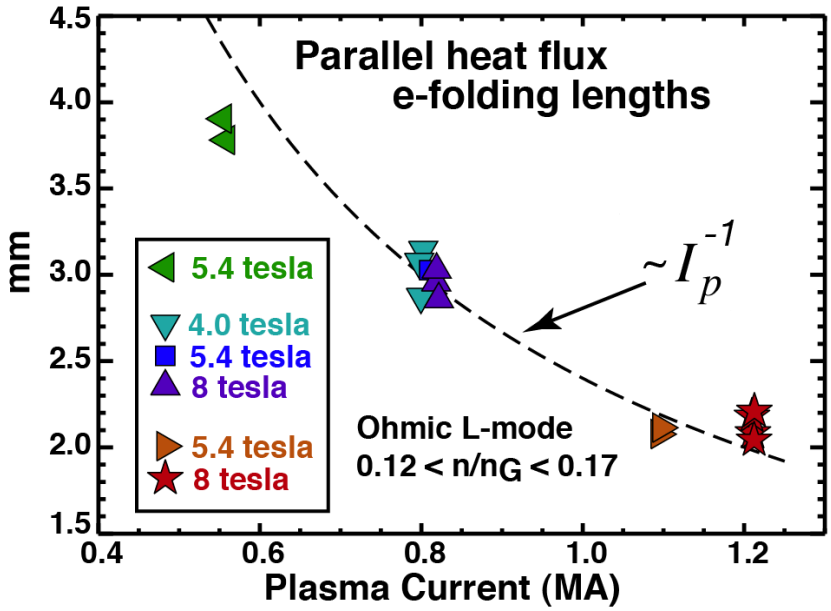

Fig. 24. Parallel heat flux profile e-folding lengths on the outer divertor, plotted versus plasma current. These data show an approximately inverse scaling with plasma current and no scaling with toroidal field strength.

These data make contact with previous investigations of boundary layer pressure profiles in ohmic L-modes [29]. In that study, normalized pressure gradients 'upstream' at outer midplane (i.e., normalized by plasma current squared) were found to be invariant at a fixed collisionality; no sensitivity to magnetic field strength was detected. An in-depth analysis of these discharges is presently underway, with the goal of presented the latest results at the 2010 November APS meeting.

7. Measurements of Boundary Layer Turbulence

We are not able to predict heat-flux widths from first-principles' theory and modeling. This is the case partly because turbulent transport – also not yet predicted from first principles' modeling - no doubt plays an important role in setting this important measure. The study of the edge and SOL turbulence was therefore recognized as an essential part of this JRT research; diagnostics sensitive to turbulence in the edge and SOL were engaged for almost all of the runs dedicated to the heat-flux footprint investigations. On C-Mod, Gas-Puff-Imaging (GPI) was the primary turbulence diagnostic in the study. Phase Contrast Imaging (PCI) and three scanning Langmuir probes were also active turbulence diagnostics. Two GPI systems view the outboard edge of the plasma near the plasma midplane. One is a 9x10 array of views coupled to Avalanche Photo-Diodes (APDs)[30]. Each view images a 3.5 mm diameter spot in the (R,θ) plane at the toroidal location of a local gas-puff nozzle. This sensitive, low-noise system has a Nyquist frequency of 1 MHz. The second GPI system images a 2D region slightly larger that that viewed by the APD array onto an ultra-fast framing camera. The spatial resolution of the camera imaging is ~2 mm. Over the course of these experiments, cameras with maximum Nyquist frequencies of 125 kHz and 200 kHz were employed. The camera views the plasma with sightlines approximately aligned with the local magnetic field when q_{95}=3.5, while the APD system views are purely toroidal. Some of the results are summarized here, although much of the turbulence data is still being analyzed.

We make the distinction in this section between the 'edge region', i.e. the region ~2 cm just inside the separatrix, and the 'near' and 'far' SOL. The near SOL is the ~3 mm just beyond the separatrix carrying most of the parallel SOL heat-flux, and the far SOL is the region beyond that where blobs/filaments are the dominant manifestation of particle transport. The edge region also contains the pedestal of H-mode plasmas. Figure 25 shows these regions, as well as a raw image from the GPI fast-camera containing a clear 'blobby' transport event.

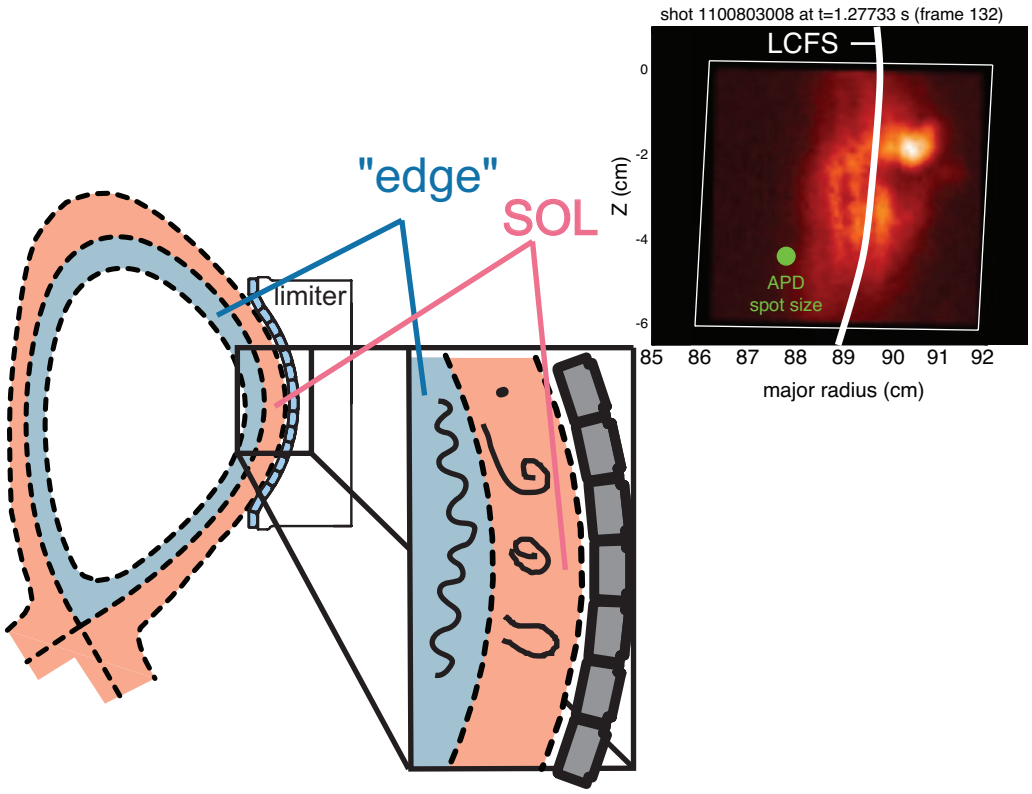

Fig. 25. Schematic of edge and SOL regions in GPI diagnostics' views, illustrating "wavelike" turbulence in the edge emerging as blobs and propagating out through the SOL. In the upper right is a raw GPI camera image with a blob present in the SOL at R_{maj}~90.5 cm.

7.1 Turbulence near the last-closed flux surface

It is reasonable to ask why we are investigating the turbulence in the *edge* (in addition to the SOL), when the heat-flux width in the SOL and footprint on the target are the primary subjects of interest. The answers to that question are: (1) there is evidence (see section 5.4) that the pedestal transport "spills over" into the near SOL affecting the heat flux width, and we seek to determine the physics of this phenomenon, (2) the edge fluctuation dominating the pedestal particle transport in EDA H-mode plasmas is the Quasi-Coherent Mode (QCM) [31], and, while the QCM is strongest in the edge region, GPI measurements show that it extends into the near SOL, and (3) both the H-mode pedestal [25] and the near SOL [29] exhibit "critical-gradient"-like transport responses, i.e., pressure gradients normalized by the square of the poloidal field ($\alpha_{MHD} = 2\mu_o R \nabla p/B_p^2$) tend to be invariant for the same value of normalized (inverse) collisionality parameter ($\alpha_d \sim 1/q \times (\lambda_{ei}/R)^{0.5}$). This behavior is shown for both the pedestal and the near SOL in Figure 26.

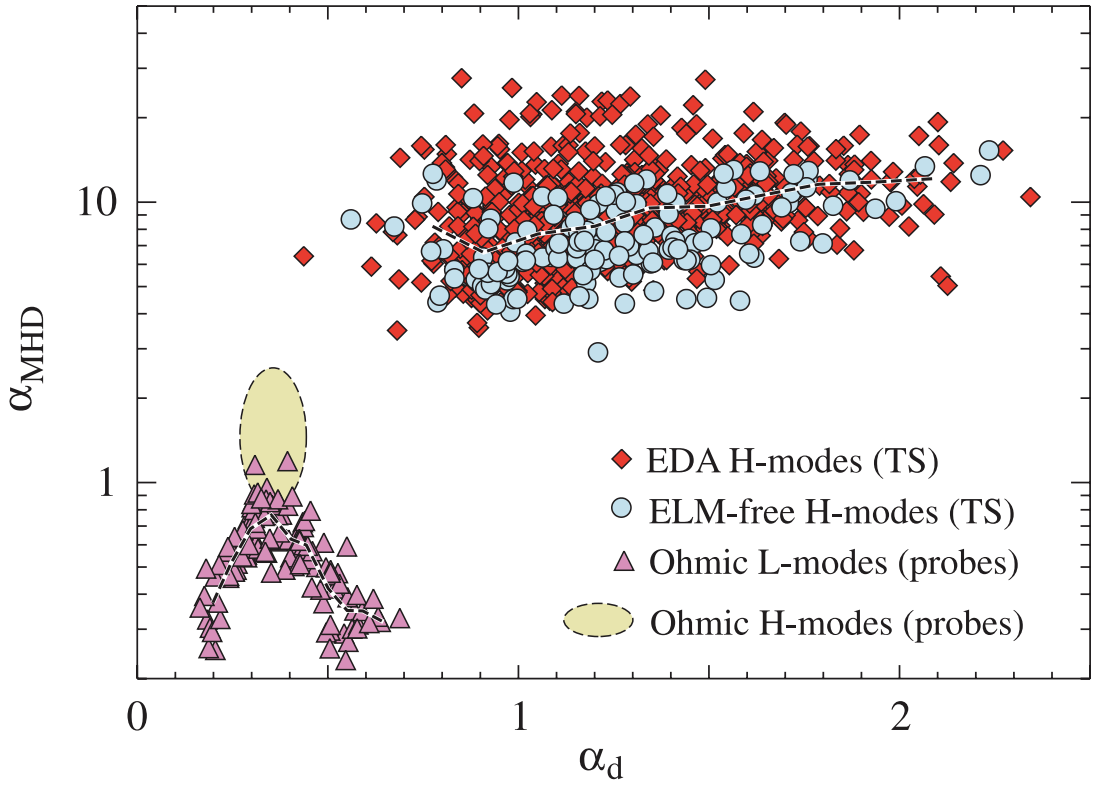

Fig. 26. Near SOL (using probes) and H-mode pedestal data cast into a dimensionless phase space suggested by electromagnetic fluid drift turbulence theory. SOL data are taken at the point of minimum pressure gradient scale length in the near SOL of ohmic discharges with I_P ranging from 0.5 to 1.0 MA. H-mode points are from discharges with 0.4 < I_P < 1.7 MA at various B_ϕ. The dashed lines represent the median value of measured α_{MHD} as a function of α_d (from [25]).

The QCM has been shown to be localized in the edge region, although GPI measurements also show that it extends into the near SOL. The QCM has also been shown to affect particle transport through the pedestal, increasing the particle loss rate over ELM-free H-mode levels, such that core density and impurity levels are regulated and held nearly constant in time. Evidence of this role in edge particle transport is shown in Fig. 27. The QCM is measured by GPI to be a mode propagating in the electron diamagnetic drift direction with k_{pol}^{QCM} ρ_s~0.1. A typical conditional (k_{pol},f) spectrum of the GPI edge fluctuations during EDA H-mode is shown in Fig. 28. The changes that occur in the frequency spectra of the electron-diamagnetic drift-directed (EDD) fluctuations through the transitions from L-mode to ELM-free H-mode to EDA H-mode are shown in Figure 28. The ~x10 increase in the fluctuation levels in going from ELM-free to EDA is further evidence for

the QCM and EDD turbulence in the edge driving particle transport. Of special interest for this work is the role of the QCM in the heat-flux width; this is presently under investigation.

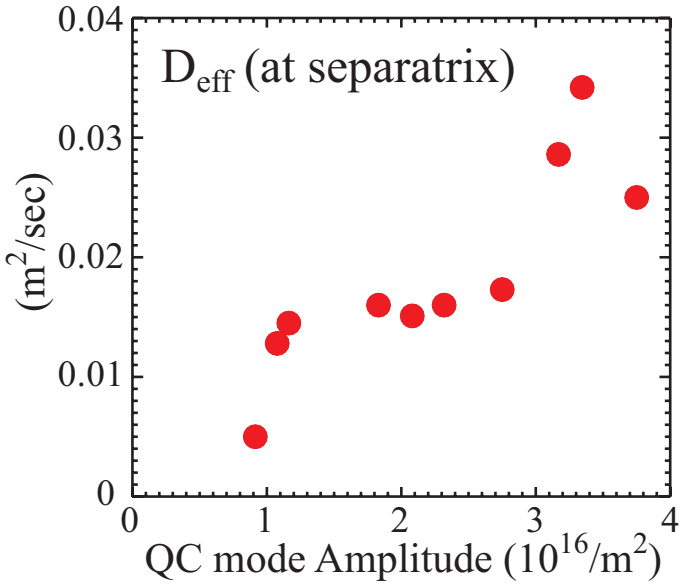

Fig. 27. Increase of D_{eff} with the increase of the QCM amplitude. Here $D_{eff} \equiv - \Gamma_{perp}/\nabla n_e$, ∇n_e, is determined from probe measurements and Γ_{perp} is inferred from spatially-resolved measurements of the ionization source. The QCM amplitude is the line integral of the density fluctuation within the QCM frequency feature (from [30]).

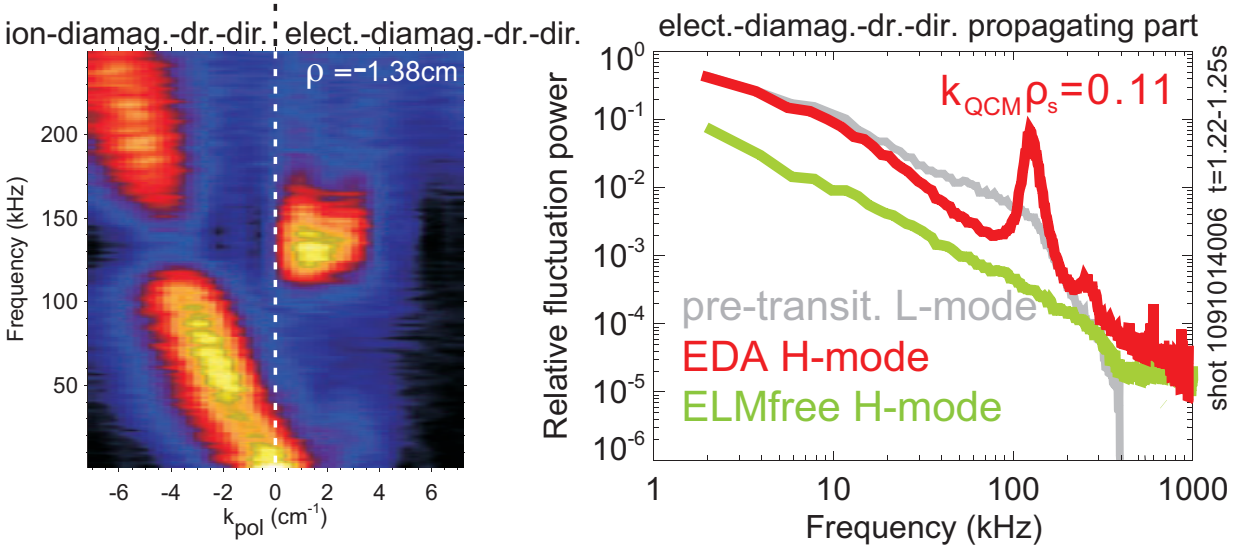

Fig. 28. Left – conditional ($k_{pol}f$) spectrogram of the edge turbulence in an ICRF-heated EDA H-mode, showing the EDD propagating QCM, as well as broadband turbulence propagating in the ion-diamagnetic-drift direction. Right – spectra of the EDD edge turbulence in the pre-H-mode phase (gray), the ELM-free H-mode phase (green), and the EDA H-mode phase (red) with the QCM at f=130 kHz. Note the ~x10 decrease in the fluctuation level in ELM-free H-mode.

In L-mode discharges the QCM is not seen, but turbulence with similar size scales is present under these conditions as well. Bispectral analyses of the spectra show that the energy input to the EDD fluctuations is occurring with the same spatial scale for both L- and EDA H-modes, i.e. with k_{pol}^{input} ρ_s~0.1. The evolution of the EDD turbulence as a function of normalized density in L-mode is shown in Figure 29.

As is evident, the power in the EDD edge turbulence increases with increased normalized density and/or with increased β_p, plotted in Figure 30. The particle flux through the SOL also increases with these parameters, as can be seen in Figure 31. We take this as additional evidence that the *EDD edge* turbulence is responsible for transport into the SOL.

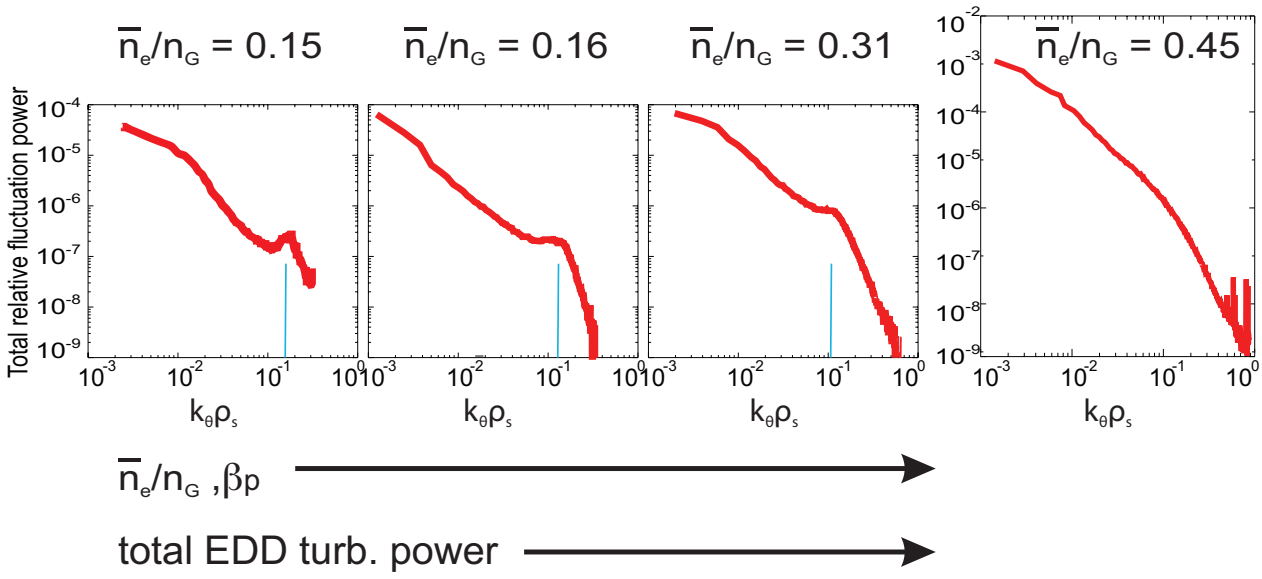

Fig. 29. The total spectral power in the EDD edge turbulence shows a strong dependence on normalized density, n_e/n_G, and on β_p (see Fig. 30) in L-mode discharges. The spectral distribution also shows strong dependence on these quantities. There is a clear local maximum or break-in-slope at k_{pol} ρ_s~0.1 in each of these spectra (blue line). Bispectral analyses of the spectra show that the energy input to the EDD turbulence has the same spatial scale for both L- and EDA H-modes.

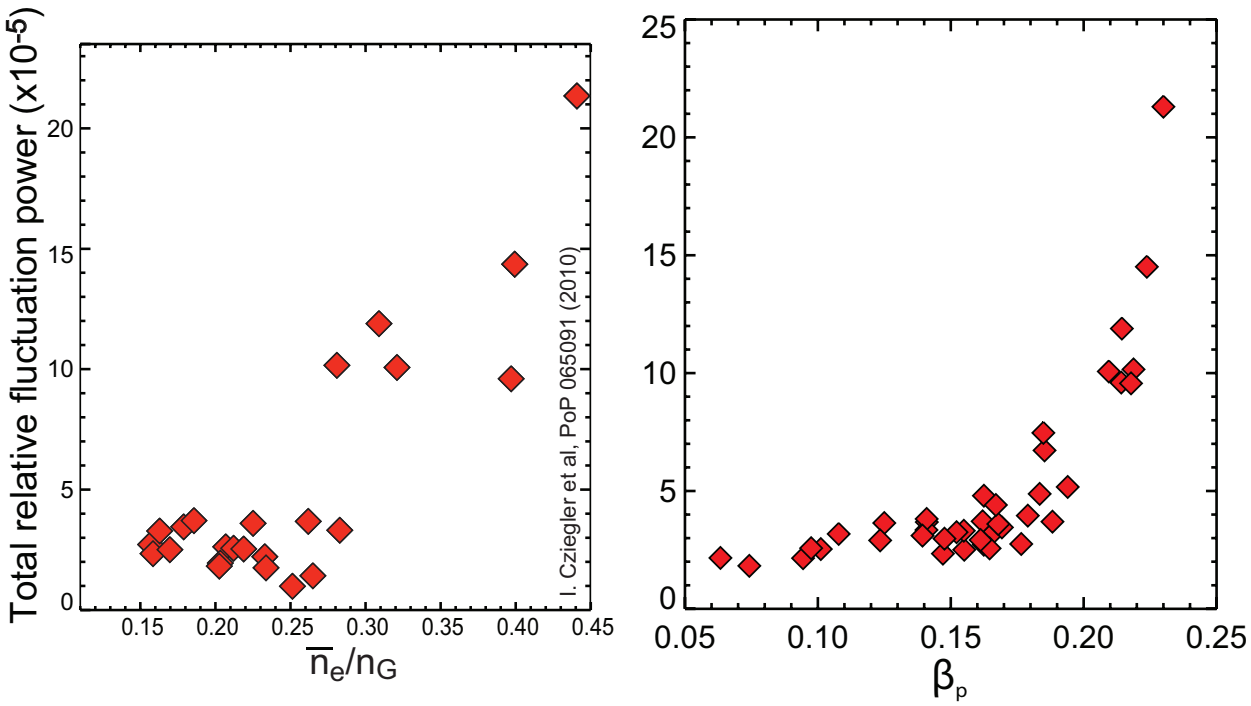

Fig. 30. (left) Power in the EED edge turbulence vs normalized density, n_e/n_G. (right) Power in the EED edge turbulence vs β_p. The physical variable β_p seems to parameterize the increase in turbulence power more sensitively than n_e/n_G.

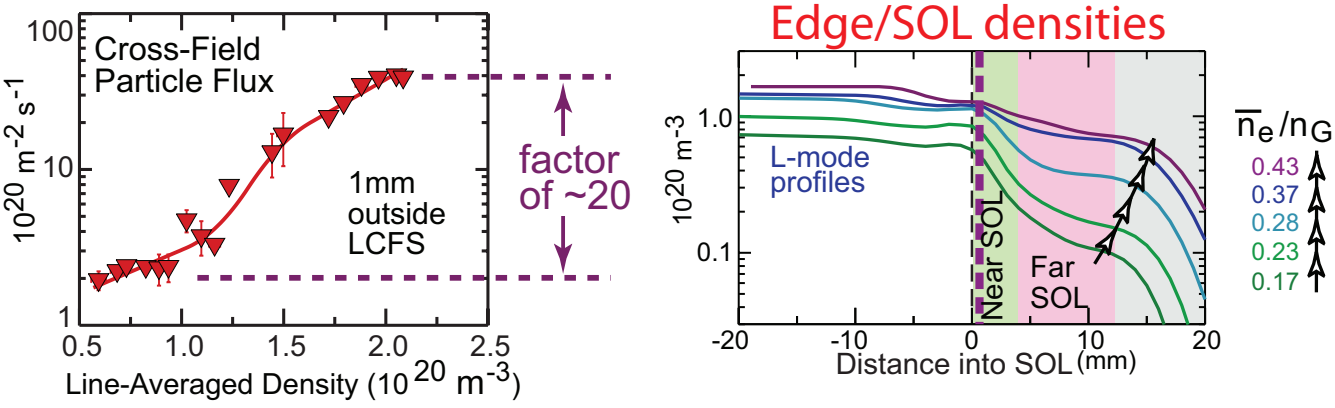

Fig. 31. Changes seen in the near SOL flux (left) and the SOL density profiles (right) as a function of normalized density. Combined with the scaling of the EDD edge turbulence shown in Fig. 27, we interpret the large increases in particle fluxes into the SOL shown here as evidence that the EDD propagating edge turbulence is a major driver of transport into the SOL.

7.2 Turbulence in the Far SOL

Far SOL turbulence is dominated by blobs and blob transport. An analysis of GPI camera data from the far SOL has been done [31] in order to estimate the effect of the convective radial

transport of SOL turbulence on the SOL density scale length, λ_n. Results were obtained for a series of ohmic discharges covering I=0.4-1.1 MA at constant q_{95} and moderate density. The average radial turbulence speed within ρ=1-2 cm near the outer midplane was calculated by a 2-D cross-correlation technique to be V_r~0.2-0.3 km/sec. Assuming this to be the local convective plasma velocity, the SOL density scale length was evaluated using a simple convective model to be λ_n~ 4-7 cm, which is ~2-3 times higher than that measured using one of the scanning Langmuir probes (see Fig. 32). The GPI-derived result has at least a factor-of two uncertainty; for example, the average parallel connection length is taken to be L_{II}~ 5 m, but is actually varying by a factor-of-two over ρ=1-2 cm, and is also different by factor-of-two in the two different directions along the magnetic field. The probe-derived results for λ_n are also uncertain by up to a factor-of-two. Thus the level of disagreement shown in Fig. 32 is not too surprising, given these uncertainties. We also note that the convective velocity measured this way is ~2-3 times lower than the velocities estimated from analytic blob-dynamic models [32-34], but exhibits a scaling similar to the models with plasma current at constant q_{95}.

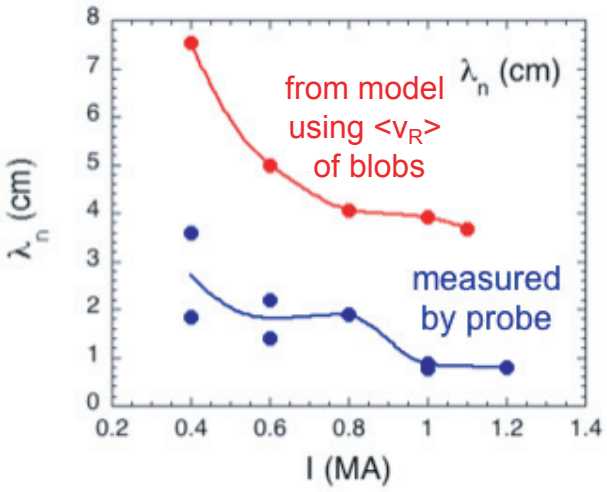

Fig. 32. The density profile scrape-off-layer scale lengths as a function of plasma current, where the scale lengths are calculated using the radial velocity of the emission structures (see text). These are compared with the scale lengths that were measured with a scanning probe. The SOL region investigated is ρ=1-2 cm.

8. Modeling activities initiated through external collaborations

Guidance from theoretical models and numerical simulations is essential to understand the physics that determines the heat-flux footprint widths in tokamaks. As stated in the FY2010 milestone text, an important component of the JRT was to generate high-quality data that could be

compared with theory and simulation. Indeed, representatives of the theory/modeling community participated fully in the JRT organizational meetings, the experimental planning and the discussions of initial results that were obtained by the three experiments. At C-Mod, special provisions were made to share experimental data directly with interested external modeling groups. In order to facilitate this, a data receptacle was set up where all processed data files relevant to modeling efforts were placed. This framework for data storage and transfer will help support subsequent JRT modeling efforts. Local directories were organized according to the C-Mod discharge (shot number) and time-in-the-discharge. With each data set were associated an ASCII file, an IDL save set file, and an explanatory text file. In addition to the experimental values, the files contained explanations of what the tabulated quantities were, the units of the quantities, how and when the files were generated. At the present time directories for three key shot/time-slices have been populated. The directory files for the relevant time-slices were subsequently e-mailed to the participating modeling groups. In parallel, we are evaluating different methods for sharing this data repository directly over the internet with our external collaborators.

The groups that are presently participating in the modeling of C-Mod JRT results are (in no particular order), the Center for Plasma Edge Simulation (CPES) group using the XGC0 code, Gary Porter (LLNL) using the UEDGE code, D. D'Ippolito, J. Myra, and D. Russell of Lodestar Corporation using the SOLT code, and R. Goldston (PPPL) using analytical modeling of parallel and perpendicular heat-flux. Results from initial modeling efforts are reported by each group in individual sections of the FY2010 JRT final report. Here we summarize the set of C-Mod experiments that were targeted for modeling and the data that were supplied to these groups.

CPES – using the XGC0 code, a time-slice from the C-Mod/DIIID similarity discharge (see Sections 5.1 and 5.2) is being modeled. Supplied processed data were: core, edge, and SOL profiles of n_e and T_e, high-resolution EFIT equilibrium, profiles of heating powers, radiated power profile, toroidal rotation profile, and Zeff.

LLNL – using the UEDGE code, a time-slice from the C-Mod/DIIID similarity discharge is being modeled. Supplied processed data were: edge and SOL profiles of n_e and T_e, high-resolution EFIT equilibrium, heat-flux profile on the outer target, and divertor Langmuir probe measurements.

Lodestar Corp. – using the SOLT turbulence code, two time-slices (EDA 1 and EDA 2 – see Section 5.4) from an EDA H-mode discharge are being modeled. Supplied processed data were: edge and SOL profiles of n_e, T_e, the profiles of the connection lengths in the SOL, P_{SOL}, profiles of

B_t and B_p. Future work with this group will include the exchange of measured and simulated GPI images, GPI analyses, as well as additional modeling of L-mode discharges of varying plasma currents, toroidal magnetic fields and collisionalities (i.e., a subset of the discharges presented in section 6).

R. Goldston – Dr. Goldston's research on the subject on heat-flux parallel and perpendicular to B was published in references[12, 35]. He visited C-Mod in March 2010 and discussed his ideas and research with C-Mod staff. Subsequent communications with C-Mod centered around ideas about how to determine the separatrix location from power balance arguments and about the heat-flux on leading edges on material surfaces that are intersected by open field lines (so-called "scrapers").

Acknowledgements

We wish to thank the entire Alcator C-Mod team for their excellent work that makes these experiments possible. This research is supported by U.S. D.o.E. Coop. Agreement DE-FC02-99ER54512.

References

[1] Kirnev, G., Fundamenski, W., and Corrigan, G., "*Modelling of ELM-averaged power exhaust on JET using the EDGE2D code with variable transport coefficients*," Plasma Physics and Controlled Fusion 49 (2007) 689.

[2] Loarte, A., Bosch, S., Chankin, A., Clement, S., Herrmann, A., Hill, D., Itami, K., Lingertat, J., Lipschultz, B., McCormick, K., Monk, R., Porter, G.D., Shimada, M., and Sugihara, M., "*Multi-machine scaling of the divertor peak heat flux and width for L-mode and H-mode discharges*," Journal of Nuclear Materials 266-269 (1999) 587.

[3] Loarte, A., Lipschultz, B., Kukushkin, A.S., Matthews, G.F., Stangeby, P.C., Asakura, N., Counsell, G.F., Federici, G., Kallenbach, A., Krieger, K., Mahdavi, A., Philipps, V., Reiter, D., Roth, J., Strachan, J., Whyte, D., Doerner, R., Eich, T., Fundamenski, W., Herrmann, A., Fenstermacher, M., Ghendrih, P., Groth, M., Kirschner, A., Konoshima, S., LaBombard, B., Lang, P., Leonard, A.W., Monier-Garbet, P., Neu, R., Pacher, H., Pegourie, B., Pitts, R.A., Takamura, S., Terry, J., and Tsitrone, E., "*Chapter 4: Power and particle control*," Nuclear Fusion 47 (2007) S203.

[4] Kallenbach, A., Asakura, N., Kirk, A., Korotkov, A., Mahdavi, M.A., Mossessian, D., and Porter, G.D., "*Multi-machine comparisons of H-mode separatrix densities and edge profile*

behaviour in the ITPA SOL and Divertor Physics Topical Group," Journal of Nuclear Materials 337-339 (2005) 381.

[5] LaBombard, B., Terry, J.L., Hughes, J.W., Brunner, D., Payne, J., Reinke, M., Lin, Y., and Wukitch, S., "*Divertor heat flux footprints in EDA H-mode discharges on Alcator C-Mod*," accepted for publication in Journal of Nuclear Materials (2010).

[6] Maqueda, R.J., Wurden, G.A., Terry, J.L., and Stillerman, J.A., "*The new infrared imaging system on Alcator C-Mod*," Rev. Sci. Instrum. 70 (1999) 734.

[7] Terry, J.L., LaBombard, B., Brunner, D., and Payne, J., "*Measurements of heat-flux profiles on the divertor target of Alcator-C-Mod using IR thermography*," accepted for publication in Review of Scientific Instruments (2010).

[8] Brunner, D., LaBombard, B., Payne, J., and Terry, J.L., "*Comparison of heat flux measurements by IR thermography and probes in the Alcator C-Mod divertor*," to be published in Journal of Nuclear Materials (2010).

[9] LaBombard, B., Terry, J.L., Reinke, M.L., Brunner, D., and Payne, J., *MP#557: Commisioning of new divertor heat flux diagnostics*. 2009: http://www.psfc.mit.edu/cmod/operations/miniproposals/557.pdf.

[10] LaBombard, B., Terry, J.L., Reinke, M.L., Brunner, D., Payne, J., Cziegler, I., Greenwald, M., Hughes, J.W., Lipschultz, B., Whyte, D., and Zweben, S., *MP#570: Boundary layer heat transport experiments in L-mode plasmas*. 2009: http://www.psfc.mit.edu/research/alcator/miniproposals/570.pdf.

[11] LaBombard, B., Brunner, D., Payne, J., Reinke, M., Terry, J.L., Hughes, J.W., Lipschultz, B., and Whyte, D., "*Initial results from divertor heat-flux instrumentation on Alcator C-Mod*," Bull. Amer. Phys. Soc. http://meetings.aps.org/link/BAPS.2009.DPP.PP8.20 (2009).

[12] Goldston, R.J., "*Downstream heat flux profile vs. midplane T profile in tokamaks*," submitted to Journal of Nuclear Materials (2010).

[13] Algor simulation software, *http://www.algor.com/*.

[14] Hermann, A., "Limitations for divertor heat flux calculations of fast events in tokamaks," presented at the 28th EPS Conference on Controlled Fusion and Plasma Physics, Madeira, Portugal, 2001.

[15] Brunner, D., LaBombard, B., Terry, J.L., and Reinke, M., "*Measurements of plasma sheath heat flux in the Alcator C-Mod divertor*," to be presented at the November 2010 APS meeting in Chicago. (2010).

[16] LaBombard, B., Terry, J.L., Hughes, J.W., Lasnier, C., Maingi, R., Brunner, D., Payne, J., Reinke, M., Cziegler, I., Zweben, S., Lin, Y., and Wukitch, S., *MP#591: Boundary layer*

heat transport experiments in H-mode plasmas. 2010: http://www.psfc.mit.edu/research/alcator/miniproposals/591.pdf.

[17] Greenwald, M., Boivin, R., Bonoli, P., Budny, R., Fiore, C., Goetz, J., Granetz, R., Hubbard, A., Hutchinson, I., Irby, J., LaBombard, B., Lin, Y., Lipschultz, B., Marmar, E., Mazurenko, A., Mossessian, D., Sunn Pedersen, T., Pitcher, C.S., Porkolab, M., Rice, J., Rowan, W., Snipes, J., Schilling, G., Takase, Y., Terry, J., Wolfe, S., Weaver, J., Welch, B., and Wukitch, S., "*Characterization of enhanced D alpha high-confinement modes in Alcator C-Mod*," AIP. Physics of Plasmas 6 (1999) 1943.

[18] Lasnier, C.J., Boedo, J.A., Leonard, A.W., Makowski, M.A., and Watkins, J.G., *Inter-machine comparisons for heat flux scaling & ELM heat*. 2010: D3DMP No. 2010-62-02.

[19] Mossessian, D., Hubbard, A.E., Pedersen, T.S., Granetz, R.S., Boivin, R.L., Greenwald, M., Hughes, J., Irby, J., Johnson, D., LaBombard, B., Lin, Y., Mazurenko, A., Nazikian, R., Pitcher, C.S., Taylor, G., and Wolfe, S.M., "*Measurements and scalings of the H-mode pedestal on Alcator C-Mod*," IOP Publishing. Plasma Physics & Controlled Fusion 42 (2000) 27.

[20] Reinke, M.L. and Hutchinson, I., "*Two dimensional radiated power diagnostics on Alcator C-Mod*," Rev. Sci. Intrum. 79 (2008) 10F306.

[21] Soukhanovskii, V.A., Maingi, R., Gates, D.A., Menard, J.E., Paul, S.F., Raman, R., Roquemore, A.L., Bell, R.E., Bush, C.E., Kaita, R., Kugel, H.W., LeBlanc, B.P., and Mueller, D., "*Divertor heat flux mitigation in high-performance H-mode discharges in the national spherical torus experiment*," Nuclear Fusion 49 (2009) 095025 (10 pp.).

[22] Lasnier, C.J., Hill, D.N., Petrie, T.W., Leonard, A.W., Evans, T.E., and Maingi, R., "*Survey of target plate heat flux in diverted DIII-D tokamak discharges*," Nuclear Fusion 38 (1998) 1225.

[23] LaBombard, B., Rice, J.E., Hubbard, A.E., Hughes, J.W., Greenwald, M., Irby, J.H., Lin, Y., Lipschultz, B., Marmar, E.S., Smick, N., Wolfe, S.M., and Wukitch, S.J., "*Transport-Driven Scrape-off Layer Flows and the Boundary Conditions Imposed at the Magnetic Separatrix in a Tokamak Plasma*," Nuclear Fusion 44 (2004) 1047.

[24] LaBombard, B., Goetz, J.A., Hutchinson, I., Jablonski, D., Kesner, J., Kurz, C., Lipschultz, B., McCracken, G.M., Niemczewski, A., Terry, J., Allen, A., Boivin, R.L., Bombarda, F., Bonoli, P., Christensen, C., Fiore, C., Garnier, D., Golovato, S., Granetz, R., Greenwald, M., Horne, S., Hubbard, A., Irby, J., Lo, D., Lumma, D., Marmar, E., May, M., Mazurenko, A., Nachtrieb, R., Ohkawa, H., O'Shea, P., Porkolab, M., Reardon, J., Rice, J., Rost, J., Schachter, J., Snipes, J., Sorci, J., Stek, P., Takase, Y., Wang, Y., Watterson, R., Weaver, J., Welch, B., and Wolfe, S., in Plasma Physics and Controlled Fusion Research 1996 (Proc. 16th Int. Conf., Montreal, 1996), Vol. 1, IAEA, Vienna (1997) 825.

[25] Hughes, J.W., LaBombard, B., Terry, J., Hubbard, A., and Lipschultz, B., "*Edge profile stiffness and insensitivity of the density pedestal to neutral fuelling in Alcator C-Mod edge transport barriers*," Nuclear Fusion 47 (2007) 1057.

[26] Bevington, P.R., *Data reduction and error analysis for the physical sciences* (McGraw-Hill, New York, 1969).

[27] Lasnier, C., Makowski, M.A., Boedo, J.A., Allen, S.L., Brooks, N.H., Hill, D., Leonard, A.W., Watkins, J.G., and West, W.P., "*Scaling of divertor heat flux profile widths in DIII-D*," to be published in Journal of Nuclear Materials (2010).

[28] Maingi, R., *Presentation at the NSTX PAC meeting*. 2010: February 3-5, 2010.

[29] LaBombard, B., Hughes, J.W., Smick, N., Graf, A., Marr, K., McDermott, R., Reinke, M., Greenwald, M., Lipschultz, B., Terry, J.L., Whyte, D.G., and Zweben, S.J., "*Critical gradients and plasma flows in the edge plasma of Alcator C-Mod*," Physics of Plasmas 15 (2008) 056106.

[30] Terry, J.L., Basse, N.P., Cziegler, I., Greenwald, M., Grulke, O., LaBombard, B., Zweben, S., Edlund, E.M., Hughes, J.W., Lin, L., Porkolab, M., Sampsell, M., Veto, B., and Wukitch, S.J., "*Transport phenomena in the edge of Alcator C-Mod plasmas*," Nuclear Fusion 45 (2005) 1321.

[31] Zweben, S.J., Terry, J.L., LaBombard, B., Agostini, M., Greenwald, M., Grulke, O., Hughes, J.W., D'Ippolito, D.A., Krasheninnikov, S.I., Myra, J.R., Russell, D.A., Stotler, D.P., and Umansky, M., "*Estimate of Convective Radial Transport due to SOL Turbulence as Measured by GPI in Alcator C-Mod*," accepted for publication in Journal of Nuclear Materials (2010.

[32] Krasheninnikov, S.I., D'Ippolito, D.A., and Myra, J.R., "*Recent theoretical progress in understanding coherent structures in edge and SOL turbulence*," Journal of Plasma Physics 74 (2008) 679.

[33] Myra, J.R., D'Ippolito, D.A., Stotler, D.P., Zweben, S.J., LeBlanc, B.P., Menard, J.E., Maqueda, R.J., and Boedo, J., "*Blob birth and transport in the tokamak edge plasma: Analysis of imaging data*," Physics of Plasmas 13 (2006) 092509.

[34] Myra, J.R., D'Ippolito, D.A., Krasheninnikov, S.I., and Yu, G.Q., "*Convective transport in the scrape-off-layer by nonthermalized spinning blobs*," Physics of Plasmas 11 (2004) 4267.

[35] Goldston, R.J., "*Downstream heat flux profile versus midplane T profile in tokamaks*," Physics of Plasmas 17 (2010) 012503.